Chapter 1

Using X-ray as a Probe of the Terahertz Dynamics of Disordered Systems – Complementarity with Inelastic Neutron Scattering and Future Perspectives

Alessandro Cunsolo

Additional information is available at the end of the chapter

http://dx.doi.org/10.5772/62844

Abstract

This Chapter is devoted to a general introduction of the high resolution (meV) inelastic x-ray scattering (IXS) technique. This starts from a theoretical derivation of the IXS cross section and the demostration of its link with the spectrum of density fluctuations. The complementarity of this technique with the other mesocopic spectrocopy method, inelastic neutron scattering (INS) is discussed in detail by emphasizing differences and similarities both from the practical and the teorethical points of view. Along with this general discussion, examples are given of both an existing IXS spectrometer and a new-concept one to be soon in operation. Finally, the result of a recent joint INS and IXS experiment on water, taking advantage of the complementarity of these two techniques, are described in the last paragraphs.

Keywords: Inelastic neutron and X-ray scattering, dynamics of disorder materials, THz spectrocopy

1. Introduction

The study of the collective dynamics of disordered systems has been a vibrant field of research since the dawn of modern science, and yet, despite an intensive theoretical, experimental, and computational scrutiny, it still presents many unsettled aspects. The main reasons are the lack of a translational invariance in the microscopic structure of these systems and the often exceptionally complex movements of their microscopic constituents.

For instance, the interplay between collective modes and inter- and intramolecular degrees of freedom, as rotations, internal vibrations, or structural relaxation processes, is a fundamental property of the fluid, which still eludes a comprehensive understanding.

The spectrum of the density fluctuations, $S(Q,\omega)$, is a well-suited variable to test various theoretical models of the liquids' dynamics because it can be directly accessed by both conventional spectroscopic methods and molecular dynamics (MD) computer simulations.

Although the shape of $S(Q,\omega)$ is reasonably understood at macroscopic or quasi-macroscopic scales, over which the fluid appears as a continuum, its evolution beyond the continuous limit still represents a theoretical challenge. In particular, this applies to the so-called "mesoscopic" regime, corresponding to distances and timescales matching with first neighboring molecules' separations and cage oscillation periods, respectively.

From the experimental side, the study of $S(Q,\omega)$ in liquids at mesoscopic scales has been an exclusive duty of inelastic neutron scattering (INS) until almost the end of the last millennium. Nowadays, INS is a rather mature technique, which first saw the light in the mid-1950s [1]. Conversely, the other mesoscopic inelastic spectroscopy, inelastic X-ray scattering (IXS), is relatively young, having been developed only a couple of decades ago, thanks to the advent of synchrotron sources with unprecedented brilliance and parallel advances in crystal optic fabrication. This time lag mainly owes to the exceptionally small energy resolution, $\Delta E/E$, required by IXS studies of the mesoscopic [nm, millielectron volt (meV)] dynamics of fluids. Specifically, being current IXS spectrometers operated at incident energies larger than ≈ 20 keV, their ability to resolve meV energies imposes a relative energy resolution, $\Delta E/E$, at least as small as 10^{-7}.

Conversely, neutrons at low-to-moderate temperatures have 1 to 10 meV energies; therefore, even moderate $\Delta E/E$ values ($10^{-2} – 10^{-1}$) are sufficient to resolve meV collective excitations in the $S(Q,\omega)$ of liquids.

Furthermore, the IX Sintensity of materials with atomic number $Z < 4$ is dominated by photoelectric absorption, which makes this technique rather inefficient when dealing with systems with high Z.

Finally, the rapid decay of the IXS cross-section upon increasing the exchanged wave vector (Q) imposes severe intensity penalties even at intermediate Q values.

Nonetheless, the superior photon fluxes delivered by new-generation undulator sources, coupled with substantial advances in the design/fabrication of IXS spectrometers' optics, can nowadays overcompensate for the mentioned intensity limitations. Consequently, the statistical accuracy currently achieved in routine IXS measurements is unmatched by other complementary terahertz (THz) methods.

A general discussion of theoretical and practical aspects of IXS technique and in particular its applications to the study of the THz dynamics of liquids is the main purpose of this chapter, the rest of which is organized as follows. Section 2 describes brief derivation of the IXS cross-section. Section 3 discusses complementary aspects of IXS and INS methods. Section 4 proposes an example of current and future IXS spectrometers to illustrate how the latter hold the promise of a superior energy resolution. Finally, Section 5 concludes this chapter with an example of a joint INS and IXS experiment taking advantage of the complementarity of the two techniques.

http://dx.doi.org/10.5772/62844

2. The theory of IXS spectroscopy

Spectroscopy experiments are among the most powerful tools to investigate the properties of matter and have a very straightforward working principle, schematically outlined below.

A beam of particles–waves (e.g. neutron or X-rays) having narrow energy spread and angular divergence and a well-defined polarization impinges on a sample and is scattered in all directions.

A detector is used to count the particles deviated by an angle 2θ within a small solid angle $d\Omega$. Before the whole flight to the detector is accomplished, the particles may pass through some elements filtering their energy (monochromators and analyzers), angular divergence (collimators), and, in some cases, polarization (polarizers).

The whole instrument used to perform a scattering measurement is referred to as spectrometer, and its degree of complexity strongly depends, of course, on the physical problem the instrument is meant to investigate and the related requirement in collimation/monochromatization. Indeed, some optical elements cannot be included in the layout as irrelevant to the purpose of the measurement; for instance, when probing static, or structural, properties of the sample, as in diffraction experiments, there is no energy filter for the scattered beam (energy analyzer) because energy-integrated intensity is to be measured.

Regardless on the complexity of the specific experiment, the ultimate aim is to investigate the properties of the target sample through the counting of the probe particles having experienced an interaction with it through the scattering event. By virtue of this interaction event, the energy of the probe's particles may either be exchanged or remain constant, which, respectively, corresponds to the case of elastic or inelastic scattering measurements. Here the main focus is on the latter class of experiments and, in particular, on those involving X-rays as a probe and liquids as samples.

In general, it can be safely assumed that the interaction time between probe and target system is much shorter than any other timescale relevant to the experiment. In other terms, the scattering event can be schematized as an instantaneous collision between the X-ray beam and the scatterers, for example, electrons belonging to atoms or molecules of the sample.

If the scatterer is assumed fixed at the origin, infinitely massive, and at rest, the scattered electrical field at a distance $r = |\vec{r}|$ from the origin can be derived as the solution of the inhomogeneous Helmholtz equation [2]:

$$\left(\nabla^2 + k^2\right)\psi\left(\vec{r}\right) = -\delta\left(\vec{r}\right), \tag{1}$$

where " ∇^2 " is the Laplacian operator, whereas k is the wave number of the incident electromagnetic wave. At large distances from the origin, the outgoing wave is the sum of a plane

(transmitted) and a spherical wave. At finite scattering angles, the state of the scattered photons can be described by a spherical wave:

$$\psi_{\mathrm{sc}} \propto \frac{\mathrm{e}^{ikr}}{r}. \tag{2}$$

In summary, one can see that by virtue of the scattering event, photons are partly removed from the plane wave and re-radiated in a spherical wave, which can be thought as a simple manifestation of the Huygens' principle [3]. The photon scattered at an angle 2θ within a solid angle $\mathrm{d}\Omega$ passes though the energy filter (analyzer) and is ultimately counted by the detector after impinging on its sensitive area $\mathrm{d}A = r^2\mathrm{d}\Omega$, which is here intended to be small enough to safely approximate the scattered wave impinging on it as a plane wave (see Figure 1). The intensity scattered within a solid angle $\mathrm{d}\Omega$ and an energy spread $\mathrm{d}E_{\mathrm{F}}$ has the following general form:

$$I = KI_0 \frac{\partial^2\sigma}{\partial\Omega\,\partial E_{\mathrm{F}}}\mathrm{d}\Omega\,\mathrm{d}E_{\mathrm{F}}, \tag{3}$$

where I_0 is the intensity of the beam impinging on the sample and K is a coefficient taking into account detector efficiency, sample self-absorption, and all geometrical and/or spurious intensity effects. In the above formula, the double differential scattering cross-section was introduced:

$$\frac{\partial^2\sigma}{\partial\Omega\,\partial E'} = \frac{\text{Rate of photons scattered into } \mathrm{d}\Omega \text{ with final energy between } E' \text{ and } E' + \mathrm{d}E'}{I_0 \partial\Omega\,\partial E'}. \tag{4}$$

To derive an explicit expression for the double the variable above, it is useful to start from the Hamiltonian describing the interaction between the electrons of the target system and the time dependent electromagnetic field impinging on them. In the non-relativistic case, such an Hamiltonian reads as follows [4]:

$$H = \frac{1}{2m_e}\sum_i \left[\vec{P}_i - \frac{e}{c}\vec{A}\left(r_i\right)\delta\left(\vec{r} - \vec{r}_i\right)\right]\cdot\left[\vec{P}_i - \frac{e}{c}\vec{A}\left(r_i\right)\delta\left(\vec{r} - \vec{r}_i\right)\right] + \sum_i V\left(r_i\right) + V_{\mathrm{int}}^{\mathrm{e-e}}, \tag{5}$$

where $\vec{P}_i$ and $\vec{r}_i$ represent the momentum and the position of the ith electron, respectively; c, e, and m_{e} are the speed of light in vacuum, the electron charge, and mass, respectively; $\vec{A}(\vec{r})$ is the vector potential at the position $\vec{r}$ and finally, $V_{\mathrm{int}}^{\mathrm{e-e}}$ is the electron–electron interaction integrated over the electron clouds of target atoms.

http://dx.doi.org/10.5772/62844

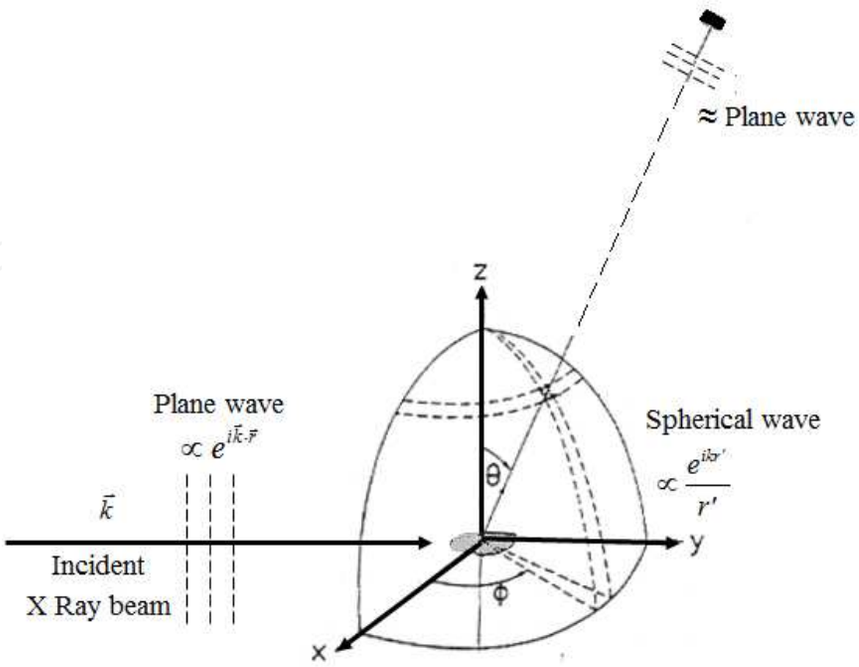

Figure 1. Schematic representation of the scattering geometry.

In Eq. 5, all the spin-dependent contributions are omitted because, in general, those couple very weakly with the incident electromagnetic field. The Hamiltonian in Eq. 5 can be cast as follows:

$$
\begin{aligned}
&H = H_{\mathrm{el}} + H_{\mathrm{int}}^{(1)} + H_{\mathrm{int}}^{(2)},\\
&\text{where}\\
&H_{\mathrm{el}} = \sum_i \left[\frac{P_i^2}{2M} + V(r_i) \right] && \text{(a)}\\
&H_{\mathrm{int}}^{1} = -\frac{e}{2mc} \sum_i \left[\vec{P}_i \cdot \vec{A}(\vec{r}) \delta\left(\vec{r} - \vec{r}_i\right) + \vec{A}\delta\left(\vec{r} - \vec{r}_i\right) \cdot \vec{P}_i \right] && \text{(b)}\\
&H_{\mathrm{int}}^{2} = \frac{e^2}{2mc^2} \sum_i \delta\left(\vec{r} - \vec{r}_i\right) \vec{A}(\vec{r}) \cdot \vec{A}(\vec{r}) && \text{(c)}
\end{aligned}
\qquad (6)
$$

On a general ground, the parts containing the square of the perturbing term, i.e. the vector potential, contribute to two-photon processes such as the scattering event. The two terms entering in H_{int}^{1} (Eq. 6b), both being linear in $\vec{A}(\vec{r})$, describe to the leading order one-photon processes, such as absorption and emission, while they account for the scattering process to the second order only. Conversely, the so-called Thomson term, i.e. the term H_{int}^{2} in Eq. 6c, being quadratic in the vector potential, accounts to the first order for a two-photon process, such as the scattering event. It can be shown that, away from an energy resonance, the Thomson term dominates over the second-order expansion of Eq. 6b, thus providing the leading

contribution to the scattering process. In the following, an explicit derivation of the double differential IXS cross section is carried out within the assumption that the Thomson term entirely describes the scattering process and further assuming that:

- The center of mass of the electronic cloud follows the nuclear motion as a slow drift, i.e. with no delay (adiabatic approximation). This justifies the expression of the initial and final states of scatterer as the product of two terms containing either only electronic or only nuclear coordinates. This approximation becomes particularly accurate at energies smaller than excitation energies of electrons in bound core states, i.e. for nearly all cases of practical interest for high resolution IXS measurements. In liquid metals, this approximation only excludes electron densities near the Fermi level.
- The electronic part of the total wave function is unaffected by the scattering process, thus the difference between the initial (before scattering) state and the final (after scattering) state is due only to excitations associated with atomic density fluctuations.

The following derivation can be found in various textbooks and is also clearly illustrated in a theoretical work by Sinha [4], whose main results are discussed here.

In principle, one could use the perturbation theory to derive the rate of scattering events associated to an incident plane wave having wave vector $\vec{k}_I$ and to all plane waves having wave vector $\vec{k}_F$, pointing to a given direction 2θ within the solid angle $d\Omega$ intercepted by the detector. However, the normalization of the scattered wave would require its amplitude to decrease at least as r^{-1} at large distances r from the scattering event, and this hardly fits the case of a plane wave. To circumvent this problem, it is useful to define the scattering process within a box of size L with periodic boundary conditions and eventually consider the limit of large L. This expedient enables to easily count the states and properly normalize the wave functions.

Within such a box, the vector potential can be expressed as a linear combination of normalized plane waves of the form $1/L^{3/2}\exp(i\vec{k}\cdot\vec{r})$. Namely:

$$\vec{A}(\vec{r}) = \sum_{k,\varepsilon}\sqrt{\left(\frac{\hbar}{\omega_k L^3}\right)}c\hat{\varepsilon}\left[\vec{a}^{+}_{k,\varepsilon}\exp\left(i\vec{k}\cdot\vec{r}\right) + \vec{a}^{-}_{k,\varepsilon}\exp\left(-i\vec{k}\cdot\vec{r}\right)\right], \tag{7}$$

where the exponential with either the sign "+" or "–" describes downstream and upstream propagating plane waves, respectively. Here $\eta = h/2\pi$, where h is the Planck constant, while the indexes k and ε label, respectively, the wave vector and the polarization states of the wave, as identified by the unit vector $\hat{\varepsilon}$ and the vector $\vec{k}$, respectively. The coefficients $\vec{a}^{+}_{k,\varepsilon}$ and $\vec{a}^{-}_{k,\varepsilon}$ in Eq. 7 represent, respectively, the annihilation and the creation operators for the initial photon state $|k,\ \varepsilon\rangle$, while ω_k is the angular frequency.

The scattering process can be depicted as a simultaneous transition between the $|k_I,\varepsilon_I\rangle$ and $|k_F,\varepsilon_F\rangle$ photon states and between the $|\lambda_I\rangle$ and $|\lambda_F\rangle$ sample states. The rate of such a transition is predicted by Fermi's golden rule [5]:

http://dx.doi.org/10.5772/62844

$$\sum_{k_F}^{d\Omega} W_{|I\rangle\to|F\rangle} = \frac{2\pi}{\hbar} \nu_{k_F,\varepsilon_F} \left| \left\langle F \left| H_{int}^{(2)} \right| I \right\rangle \right|^2, \tag{8}$$

where, to ease the notation, it is assumed $|I\rangle = |k_I, \varepsilon_I, \lambda_I\rangle$, $|F\rangle = |k_F, \varepsilon_F, \lambda_F\rangle$. The parameters ν_{k_F,ε_F} represent the density of final photon states and can be derived by evaluating the density of k_F points in the reciprocal space. For this purpose, one can consider all plane waves having energies included in between E_F and $E_F + dE_F$ and pointing toward a direction 2θ within the solid angle $d\Omega$, the number of such plane waves being $\nu_{k_F,\varepsilon_F} dE_F$. In the reciprocal space, the energy spread dE_F corresponds to the volume $dV(k_F)$ of the spherical shell (see Figure 2), which is identified by vectors $\vec{k}_F$ having amplitude included in between k_F and $k_F + dk_F$ and direction included within a solid angle $d\Omega$. This elemental volume reads as follows:

$$dV(k_F) = d\Omega\, k_F^2 dk_F.$$

The k_F values included within the box defined above are given by $2\pi/L(n_x, n_y, n_z)$, with $n_{s=x,y,z}$ generic integers. This defines a lattice in the k space whose points can be associated with a unit cell of volume $V_{min} = (2\pi/L)^3$. Assuming a small cell (a large size box L), the total number of lattice points inside the elemental volume $dV(k_F)$ is given by the ratio between such a volume and V_{min}, and this must be equal to the number of plane waves defined above, that is:

$$\nu_{k_F,\varepsilon_F} dE_F = d\Omega\, k_F^2 \left(\frac{L}{2\pi}\right)^3 dk_F\ . \tag{9}$$

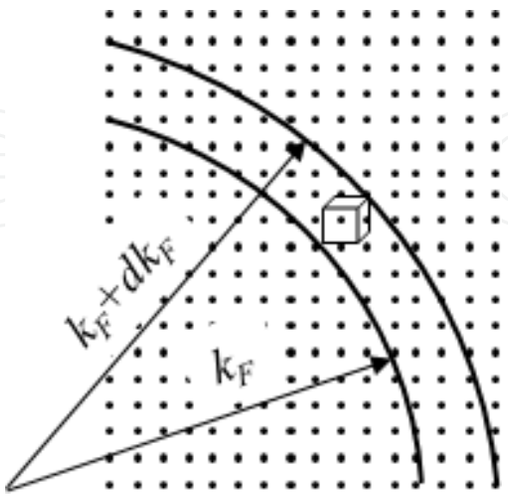

Figure 2. Schematic representation of the elemental volumes in the reciprocal space. The cube enclosing a lattice point represents the unit cell of volume $V_{min} = (2\pi/L)^3$.

$$\nu_{k_F,\varepsilon_F} dE_F = d\Omega\, k_F^2 \left(\frac{L}{2\pi}\right)^3 dk_F \ . \tag{10}$$

Furthermore, being $E_F=\hbar c k_F$, or, equivalently, $dE_F=\hbar c\, dk_F$, one has:

$$\nu_{k_F,\varepsilon_F} \mathrm{d}E_F = \frac{k_F^2 L^3}{(2\pi)^3 \hbar c} \mathrm{d}\Omega \ . \tag{11}$$

Also, the incident photon flux, i.e. the number of photons passing through a unit surface in the unit time, is given by:

$$\varphi = \frac{c}{V} \ . \tag{12}$$

Furthermore, the double differential cross section for the scattering process can be related to such a flux through:

$$\left(\frac{\mathrm{d}\sigma}{\mathrm{d}\Omega \mathrm{d}E_F}\right)_{|I\rangle\to|F\rangle} = \frac{1}{\varphi}\frac{1}{\mathrm{d}\Omega}\sum_{k_F}^{\mathrm{d}\Omega} W_{\lambda_I\to\lambda_F} \ . \tag{13}$$

Using Eqs. 8–12, the matrix element defining Fermi's golden rule (Eq. 8) can be thus expressed as:

$$\left\langle F\left|H_{\mathrm{int}}^{(2)}\right|I\right\rangle = \frac{1}{L^3}\frac{e^2}{mc^2}\frac{\hbar c}{\left[\omega(k_I)\omega(k_I)\right]^{1/2}}\left(\hat{\varepsilon}_I\cdot\hat{\varepsilon}_F\right)\left\langle \lambda_F\left|\sum_j \exp\left(-i(\vec{Q}\cdot\vec{r}_j\right)\right|\lambda_I\right\rangle \delta\left(\hbar\omega - E_I - E_F\right) \ , \tag{14}$$

Here the conservation laws of momentum and energy in the scattering event have been superimposed by assuming $\hbar\vec{Q}=\hbar(\vec{k}_F-\vec{k}_I)$ and $\hbar\omega=E_F-E_I$, with $\hbar\vec{Q}$ and $\hbar\omega$ being the momentum and energy transferred from the photon to the target sample. In particular, the energy conservation is accounted by the $\delta(\hbar\omega-E_I-E_F)$ term in Eq. 13. Considering that the frequency of the incident (scattered) wave is $\omega(k_I)=ck_I$ ($\omega(k_F)=ck_F$), the double differential cross-section reduces to:

$$\begin{aligned}\left(\frac{\mathrm{d}^2\sigma}{\mathrm{d}\Omega \mathrm{d}E'}\right)_{|I\rangle\to|F\rangle} &= \frac{e^2}{mc^2}\left(\frac{k'}{k}\right)\left(\hat{\varepsilon}_I\cdot\hat{\varepsilon}_F\right)\times \\ \times\sum_{mj}&\left[\left\langle\lambda_I\left|\exp\left(-i\vec{Q}\cdot\vec{r}_m\right)\right|\lambda_F\right\rangle\left\langle\lambda_F\left|\exp\left(i\vec{Q}\cdot\vec{r}_j\right)\right|\lambda_I\right\rangle\right]\delta\left(\hbar\omega+E_I-E_F\right) \ .\end{aligned} \tag{15}$$

http://dx.doi.org/10.5772/62844

It has to be noticed that the sum involves states of the target system only. Here the indexes "m" and "j" label the coordinates of the scatterers, i.e. the electrons interacting with the electromagnetic field.

In a scattering experiment, the states of the target system $|\lambda_I\rangle$ and $|\lambda_F\rangle$ are generally unknown, because only the final and initial states of the photons are measured. However, it is usually assumed that, before the scattering event, the sample is in its thermodynamic equilibrium and, therefore, a "thermal" average can be performed over its initial state. Furthermore, if the sample can be treated as a many-body classical system, the probability of the $|\lambda_I\rangle$ state is $p_I=\exp(-\beta E_I)\Big/\sum_I \exp(-\beta E_I)$, where $\beta = 1/k_B T$ and k_B and T are the Boltzmann constant and the temperature of the sample, respectively. At this stage, the cross section associated to the transition between the photon states $|k_I, \varepsilon_I\rangle$ and $|k_F, \varepsilon_F\rangle$ can be written as:

$$\left(\frac{\mathrm{d}^2\sigma}{\mathrm{d}\Omega \mathrm{d}E_F}\right)_{|k_I,\varepsilon_I\rangle\to k_F,\varepsilon_F\rangle} = \frac{e^2}{mc^2}\left(\frac{k_F}{k_I}\right)\left(\hat{\varepsilon}_I\cdot\hat{\varepsilon}_F\right)\times$$
$$\times\sum_{mj}\sum_{\lambda_I\lambda_F}\left[p_\lambda\left\langle\lambda_I\left|\exp\left(-i\vec{Q}\cdot\vec{r}_m\right)\right|\lambda_F\right\rangle\left\langle\lambda_F\left|\exp\left(i\vec{Q}\cdot\vec{r}_j\right)\right|\lambda_I\right\rangle\right]\delta\left(\hbar\omega+E_I-E_F\right). \tag{16}$$

This formula can be further simplified by:

- assuming the completeness of the final eigenstates of the system $\sum_{\lambda_F}|\lambda_F\rangle\langle\lambda_F| = I$, with I being the identity operator,
- considering that

$$\delta(\hbar\omega + E_I - E_F) = 1/2\pi\hbar\int_{-\infty}^{\infty}\exp(i\omega t)\exp(E_I - E_F)/\hbar,$$

- using the Heisenberg representation of the time evolution of a generic operator $A(t)=\exp(iHt/\hbar)A(0)\exp(-iHt/\hbar)$, where H is the Hamiltonian of the unperturbed system, and finally
- considering that, since $|I\rangle$ and $|F\rangle$ eigenstates of the Hamiltonian, one has: $\exp(iE_I t/\hbar)|I\rangle = \exp(iHt/\hbar)|I\rangle$ and $\exp(iE_F t/\hbar)|I\rangle = \exp(iHt/\hbar)|F\rangle$.

With the above manipulations, the double differential cross section eventually reduces to:

$$\left(\frac{\mathrm{d}^2\sigma}{\mathrm{d}\Omega \mathrm{d}E'}\right)_{|k_I,\varepsilon_I\rangle\to|k_F,\varepsilon_F\rangle} = \frac{e^2}{mc^2}\left(\frac{k'}{k}\right)\left(\hat{\varepsilon}_I\cdot\hat{\varepsilon}_F\right)\times$$
$$\times\frac{1}{2\pi\hbar}\int_0^{\infty}\sum_{mj}\left\langle\exp\left\{-i\vec{Q}\cdot\left[\vec{r}_j(t)-\vec{r}_m(0)\right]\right\}\right\rangle\exp(i\omega t)\mathrm{d}t, \tag{17}$$

where the correlation function between two generic variables was introduced as:

$\langle A\langle 0\rangle B(t)\rangle = \sum_{\lambda} p_{\lambda}\langle \lambda \mid A\langle 0\rangle B(t) \mid \lambda\rangle$.was introduced.

2.1. Cross section and density correlation function

The double differential cross section can be now simply connected to the Fourier transform of the density–density correlation function, as discussed in [6].

To show this explicitly, it is useful to start from an appropriate definition of the atomic density in the mesoscopic regime probed by IXS. There, the density of a single atom can be approximated by Dirac's δ function of the space coordinate:

$$n_j(\vec{r},t) = \delta\left[\vec{r} - \vec{R}_j(t)\right]. \tag{18}$$

Clearly, this is a highly discontinuous function diverging at the center of mass position of the jth atom $\vec{R}_j(t)$ and vanishing elsewhere. The normalization condition $\int_V n_j(\vec{r},t)\mathrm{d}\vec{r} = 1$ simply means that, if a sufficiently large volume is covered, the particle should be counted one time inside such a volume. A coarse estimate of the density variable is given by the mean value $\langle n_j(\vec{r},t)\rangle = 1\Big/ V\int_V n_j(\vec{r},t)\mathrm{d}\vec{r} = 1\Big/ V$ obtained as a statistical average over a certain volume. The density function of a system of N atoms, the density function can be expressed as follows:

$$n(\vec{r},t) = \sum_{i=1}^{N}\delta\left[\vec{r} - \vec{R}_i(t)\right].$$

One can perform the average density by integrating over the volume, eventually obtaining $\left\langle n(\vec{r},t)\right\rangle = 1/V\int_V n(\vec{r},t)\mathrm{d}\vec{r} = n$, where $n=N/V$ is the number density (number of atoms in the unit volume) of the system. However, in the present context is more useful to deal with the density fluctuation:

$$\delta n(\vec{r},t) = \sum_{i=1}^{N}\delta\left[\vec{r} - \vec{R}_i(t)\right] - n. \tag{19}$$

At this stage, the atomic Van Hove correlation function can be introduced as:

$$G(\vec{r},t) = \frac{1}{N}\sum_{k,j=1}^{N}\left\langle \delta\left[\vec{r} - \vec{R}_k(0)\right]\delta\left[\vec{r} - \vec{R}_j(t)\right]\right\rangle - n = \frac{1}{N}\sum_{k,j=1}^{N}\left\langle \delta\left[\vec{r} - \vec{R}_k(0) - \vec{R}_j(t)\right]\right\rangle - n. \tag{20}$$

http://dx.doi.org/10.5772/62844

Since a scattering experiment probes the reciprocal rather than the real space, it is here convenient to introduce the Fourier transform of the density in Eq. 18:

$$\delta n\left(\vec{Q},t\right)=\sum_{j}\exp\left[\vec{r}-\vec{R}_{j}(t)\right]-\left(2\pi\right)^{3}n\delta\left(\vec{Q}\right). \tag{21}$$

and its time-correlation, the intermediate scattering function:

$$\tilde{F}(\vec{Q},t)=\langle\delta n^{*}(\vec{Q},0)\delta n(\vec{Q},t)\rangle=\frac{1}{N}\sum_{mj}\exp\left\langle i\vec{Q}\cdot\left[\vec{R}_{j}(t)-\vec{R}_{m}(0)\right]\right\rangle-\left(2\pi\right)^{3}\delta\left(\vec{Q}\right). \tag{22}$$

Finally, the dynamic structure factor, which is the variable actually measured in a scattering experiment, reads as:

$$\begin{aligned}&\tilde{S}(\vec{Q},\omega)=\frac{1}{2\pi\hbar}\int_{-\infty}^{+\infty}e^{i\omega t}\langle\delta n^{*}\left(\vec{Q},0\right)\delta n\left(\vec{Q},t\right)\rangle\,\mathrm{d}t=\\&\frac{1}{2\pi\hbar}\int_{0}^{t}\left[\sum_{mj}\exp\left\langle i\vec{Q}\cdot\left[\vec{R}_{j}(t)-\vec{R}_{m}(0)\right]\right\rangle-\left(2\pi\right)^{3}\delta\left(\vec{Q}\right)\right]\exp\left(i\omega t\right)\mathrm{d}t\ .\end{aligned} \tag{23}$$

One can easily recognize that the second term under integration (having the sign "-" as a pre-factor) is proportional to $\delta(\omega)\delta(\vec{Q})$, thus is not relevant in a real IXS or INS experiment, as it describes the merely elastic (ω=0) scattering in the forward direction ($\vec{Q}$=0). Therefore, one can make the following identification:

$$\tilde{S}(\vec{Q},\omega)\rightarrow S(\vec{Q},\omega)=\frac{1}{2\pi\hbar}\int_{0}^{t}\left[\sum_{mj}\exp\left\langle i\vec{Q}\cdot\left[\vec{R}_{j}(t)-\vec{R}_{m}(0)\right]\right\rangle\right]\exp\left(i\omega t\right)\mathrm{d}t$$

It is important to recognize that Eqs. 17–23 depend on the center of mass (nuclear) coordinates of the atoms. The integral in Eq. 16 is thus to be identified with the spectrum of the density fluctuation autocorrelation function, provided the electronic coordinates $\vec{r}_{j}(t)$ are replaced by the nuclear ones $\vec{R}_{j}(t)$. This identification relies on the validity of the Born–Oppenheimer approximation, which ultimately justifies the factorization between exponential terms containing either merely electronic or merely nuclear coordinates. With such a factorization, the double differential cross section reduces to:

$$\left(\frac{\mathrm{d}^{2}\sigma}{\mathrm{d}\Omega\mathrm{d}E'}\right)=\frac{e^{2}}{mc^{2}}\left(\frac{k'}{k}\right)\left(\hat{\varepsilon}_{\mathrm{I}}\cdot\hat{\varepsilon}_{\mathrm{F}}\right)\left|f\left(Q\right)\right|^{2}S\left(Q,\omega\right), \tag{24}$$

where

$$f(Q) = \sum_{\alpha} \exp(-i\vec{Q} \cdot \vec{\rho}_{\alpha}) \tag{25}$$

is the atomic structure factor, which depends on the coordinate $\vec{\rho}_{\alpha}$ of the αth electron in the reference frame with the nucleus at the origin. It is worth stressing that the sum in Eq. 25 runs over all electrons in the atom. Furthermore, in Eq. 24 it was assumed the isotropic character of a liquid system, which implies that physical properties do not depend on the direction of $\vec{Q}$ but only on its amplitude $Q = |\vec{Q}|$.

2.2. The incoherent contribution

The derivation discussed above strictly applies to systems of N identical atoms within the validity of the Born–Oppenheimer approximation. For a system containing different atoms, the derivation of the scattering cross section is only slightly more complex. However, a factorization between a merely electronic and a nuclear term is still possible and leads to the conclusion that the double differential cross section splits into two components: a coherent and an incoherent one. The former is proportional to the average value of the form factor, whereas the latter arises from its mean square fluctuations.

To illustrate this point, it is useful to start from the assumption that atoms in the target system have reasonably symmetric electronic clouds. The double differential cross section can thus be expressed as follows:

$$\left(\frac{\partial \sigma}{\partial \Omega \mathrm{d}E'}\right) = r_0^2 \left(\frac{k'}{k}\right) (\hat{\varepsilon}_f \cdot \hat{\varepsilon}_i)^2 \frac{1}{N} \sum_{\alpha\beta} \sum_{mj} \left\langle \exp\left[iQ \cdot \left(\vec{R}_j(t) - \vec{R}_m(0) \right) \right] \right\rangle \overline{e\exp\left[i\vec{Q} \cdot \left(\vec{\rho}_{\alpha}^{\,n} - \vec{\rho}_{\beta}^{\,m} \right) \right]}, \tag{26}$$

where the $\vec{\rho}_{\alpha}^{\,i}$ is the position the αth electron of the ith atom in the reference frame of atomic center of atomic mass. Here the bar on the top of the exponential term indicates an average over all atoms of the system. We can thus distinguish two cases in the following:

1. The term under average involves distinct atoms ($n \neq m$), then:

$$\sum_{\alpha,\beta} \overline{\exp\left(i\vec{Q} \cdot \vec{\rho}_{\alpha}^{\,n}\right) \exp\left(i\vec{Q} \cdot \vec{\rho}_{\beta}^{\,m}\right)} = \sum_{\alpha} \overline{\exp\left(i\vec{Q} \cdot \vec{\rho}_{\alpha}^{\,n}\right)} \sum_{\beta} \overline{\exp\left(i\vec{Q} \cdot \vec{\rho}_{\beta}^{\,m}\right)} = \overline{f(Q)}^2.$$

2. The term under average involves the same atom ($n = m$), then:

$$\sum_{\alpha,\beta} \overline{\exp\left(i\vec{Q} \cdot \vec{\rho}_{\alpha}^{\,n}\right) \exp\left(i\vec{Q} \cdot \vec{\rho}_{\beta}^{\,m}\right)} = \overline{f(Q)^2}.$$

http://dx.doi.org/10.5772/62844

Thus, in general:

$$\sum_{\alpha,\beta}\overline{\exp\left(i\vec{Q}\cdot\vec{\rho}_{\alpha}^{n}\right)\exp\left(i\vec{Q}\cdot\vec{\rho}_{\beta}^{m}\right)}=\overline{f\left(Q\right)^{2}}+\delta_{n,m}\left(\overline{f\left(Q\right)^{2}}-\overline{f\left(Q\right)}^{2}\right)=\overline{f\left(Q\right)^{2}}+\delta_{n,m}\overline{\left(f\left(Q\right)-\overline{f\left(Q\right)}\right)^{2}},$$

$$\overline{f\left(Q\right)^{2}}+\delta_{n,m}\left(\overline{f\left(Q\right)^{2}}-\overline{f\left(Q\right)}^{2}\right)=\overline{f\left(Q\right)^{2}}+\delta_{n,m}\overline{\left(f\left(Q\right)-\overline{f\left(Q\right)}\right)^{2}}$$

which eventually leads to the following expression for the IXS cross section:

$$\frac{\partial^{2}\sigma}{\partial\Omega\partial E_{\mathrm{F}}}=r_{0}^{2}\left(\frac{k_{\mathrm{F}}}{k_{\mathrm{I}}}\right)\left(\hat{\varepsilon}_{\mathrm{I}}\cdot\hat{\varepsilon}_{\mathrm{F}}\right)\left\{\overline{f\left(Q\right)}^{2}S_{\mathrm{C}}(Q,\omega)+\left[\overline{\left(f\left(Q\right)-\overline{f\left(Q\right)}\right)^{2}}\right]S_{\mathrm{I}}(Q,\omega)\right\}. \tag{27}$$

The above formula shows that the scattering of the sample is composed of a coherent and an incoherent part, respectively, labeled by the "*C*" and "*I*" suffixes. While the latter results from the independent scattering of isolated atoms, the former also contains *the* interference between photon waves scattered by different atoms. Insight on the collective dynamics of atoms can only be sought for in the coherent scattering, whereas both coherent and incoherent scattering convey information on the single-atom dynamics.

2.3. The absorption coefficient

When actually performing the IXS measurement, it is important to optimize the sample thickness crossed by the beam (d) so as to maximize the scattering intensity. In fact, a simple d increase, albeit increasing the number of scatterers, does not necessarily enhance the scattered intensity because it also increases the sample (self) absorption. Therefore, the optimal choice of d is the result of a trade-off between competing scattering and absorption requirements. To handle the problem on a more quantitative basis, attenuation effects should be included in the general expression of the scattering intensity as prescribed by the following formula [7]:

$$I=I_{0}\frac{\partial^{2}\sigma}{\partial\Omega\,\partial E_{\mathrm{F}}}\mathrm{d}\Omega\;\mathrm{d}E_{\mathrm{F}}\;n\;d\;\exp\left(-\mu d\right), \tag{28}$$

where I_0 is the number of incident photons per second and μ is the total absorption coefficient.

The intensity I in Eq. 27 reaches a maximum when $\partial I/\partial d=0$, i.e. for $d=1/\mu$ and, consequently, $I\propto 1/\mu$.

At the energies typical of IXS experiments, attenuation effects are dominated by the photo-electric absorption, for which $\mu\propto Z^{4}$. Consequently, for high-Z elements, μ is very large, and

therefore, the optimal sample thickness is small. Of course, the optimal d value strongly depends on the incident energy and on Z. This makes IXS, in principle, ideal to work with extremely small high Z samples, and it turns out to be a decisive advantage while dealing with samples only available in modest quantities and/or when extreme thermodynamic conditions need to be explored.

3. A closer comparison between IXS and INS techniques

In general, INS and IXS present several analogies:

1. They can be used to investigate bulk properties of materials, as opposite to more strongly interacting probes, such as electrons, which essentially convey insight on materials' surfaces.
2. They probe the dynamic response of density fluctuations through the Fourier transform of their autocorrelation function, i.e. the dynamic structure factor, $S(Q, \omega)$.
3. They are "mesoscopic" probes, i.e. they cover distances and timescales matching, respectively, first neighboring atoms' (molecules') separations and cage oscillation periods.

Other similarities emerge from the comparison of the IXS double differential cross section in Eq. 26 and its INS counterparts as derived, for instance, by [8]:

$$\left.\frac{\mathrm{d}^2\sigma}{\mathrm{d}\Omega \mathrm{d}E_\mathrm{F}}\right|_\mathrm{INS} = \frac{k_\mathrm{F}}{k_\mathrm{I}} N \left[\overline{|b|}^2 S_\mathrm{C}(Q,\omega) + \overline{|b-|b||^2} S_\mathrm{I}(Q,\omega) \right]. \tag{29}$$

It can be readily noticed that:

- For both X-ray and neutron scattering, the cross section depends on the ratio $k_\mathrm{F}/k_\mathrm{I}$. However, as discussed in the following, for IXS, this factor does not depend on frequency (energy) and can be safely approximated by 1.
- The role of the form factor $f(Q)$ in the IXS cross section mirrors the one of the scattering length b in the INS one. The main difference is their physical origin: $f(Q)$ relates to the photon–electron electromagnetic interaction, while b is connected to the neutron–nuclei interaction. As a consequence, $f(Q)$ depends on Z yet not on the atomic mass, i.e. it depends on the chemical rather than isotopic specie of the target sample. As discussed below, another fundamental difference is that $f(Q)$ sharply decreases at high exchanged momenta while b remains essentially constant.

Despite these formal similarities, the two techniques have several complementary aspects, as discussed below in some detail. This makes each of them better suited to some experiments

and less to other. A practical example of the coordinate use of these complementary methods is discussed at the end of this chapter.

3.1. Part A: advantages of IXS

3.1.1. Kinematic limitations

The conservation laws of momentum and energy lead to very different results when dealing with either neutron or X-ray probes. Let us consider the neutron case first. As mentioned, the momentum conservation law reads as:

$$\vec{Q} = \vec{k}_F - \vec{k}_I, \tag{30}$$

which can be rearranged as follows:

$$\left(\frac{Q}{k_I}\right)^2 = \left(\frac{k_F}{k_I}\right)^2 + 1 - 2\frac{k_F}{k_I}\cos 2\theta, \tag{31}$$

whereas the energy conservation law for the scattering event reads as:

$$E_F - E_I = \hbar\omega. \tag{32}$$

Considering that the kinetic energy of the freely flying neutron is:

$$E = \hbar^2 k^2 / 2m_n \tag{33}$$

with m_n being the neutron mass, Eq. 27 can be written as:

$$\left(\frac{k_F}{k_I}\right)^2 = \frac{\hbar\omega}{E_F} + 1. \tag{34}$$

By combining Eqs. 29 and 26 and taking the square root of both members, one eventually obtains:

$$\left(\frac{Q}{k_I}\right) = \sqrt{2 - \left(\frac{\hbar\omega}{E_I}\right) - 2\ \cos(2\theta)\sqrt{1 - \left(\frac{\hbar\omega}{E_I}\right)}}. \tag{35}$$

It is thus readily noticed that the dynamic domain (Q,ω) explored by an INS measurement is limited by the condition that both the arguments under the two square roots of Eq. 30 are positive. In particular, the argument of the "nested" square root, having pre-factor $2\cos(2\theta)$, is positive whenever $E_I < \hbar\omega$. This reflects the obvious requirement that the energy transferred from the neutron to the sample cannot exceed the energy E_I initially carried by the neutron. Furthermore, the requirement for the argument of the larger square root in Eq. 26 to be positive introduces further restrictions to the explored dynamic range.

An example of these restrictions, customarily referred to as kinematic limitations, is provided by Figure 3, which refers to the specific case of INS experiments on water.

It is worth recalling that, since the pioneering MD work of [9] in the mid-1970s, it is well-known that the THz spectrum of water is dominated by two inelastic peaks, whose Q dispersions are reported in Figure 3 as computed by MD simulations [10]. However, the spectrum of water measured by two successive INS works (also reported in the plot) did not bear any evidence of a double peaked shape. The reason of the apparent discrepancy between computational and experimental results mainly owed to kinematic and resolution limitations affecting the latter. These limitations were substantially different in the two measurements, owing to the different incident energies: 36 meV and 80 meV respectively for [11] and [12]. In the former experiment [11] these limitations prevented the proper coverage of the high energy modes. Conversely, the higher incident energy (barely) permitted the second INS measurement [12] to cover the high energy mode, yet it entailed a coarsening of the energy resolution, which became too broad to properly resolve the low frequency mode. For reference, Figure 3 displays the portion of the dynamic plane covered by Bosi and coworkers' measurement (shadowed area) along with the boundary of the dynamic region explored by Teixeira and coworkers' one.

Briefly, Figure 3 exemplifies a situation in which the dynamic range covered by the experiment resembles a "blanket too short" preventing the simultaneous access to both high and low ω or Q values. A similar problem is commonly encountered in INS measurements,

The development of high energy resolution (meV) IXS in the mid-1990s offered the opportunity of performing THz spectroscopy measurements virtually free from kinematic limitations, apart from the obvious ones related to the finite energy and momentum resolutions.

Such a virtual absence of kinematic constraints follows from these two circumstances:

1. the energy–momentum relationship for photons is linear:

$$E_j = ck_j \tag{36}$$

instead of quadratic, as for INS (see Eq. 28) and

2. for IXS $\hbar\omega << E_I$ (typically $E_I \approx 20$ keV, while $|\hbar\omega| \leq \approx 80$ meV), or, equivalently $E_F = E_I$, which, through Eq. 31, implies $k_F = k_I$.

http://dx.doi.org/10.5772/62844

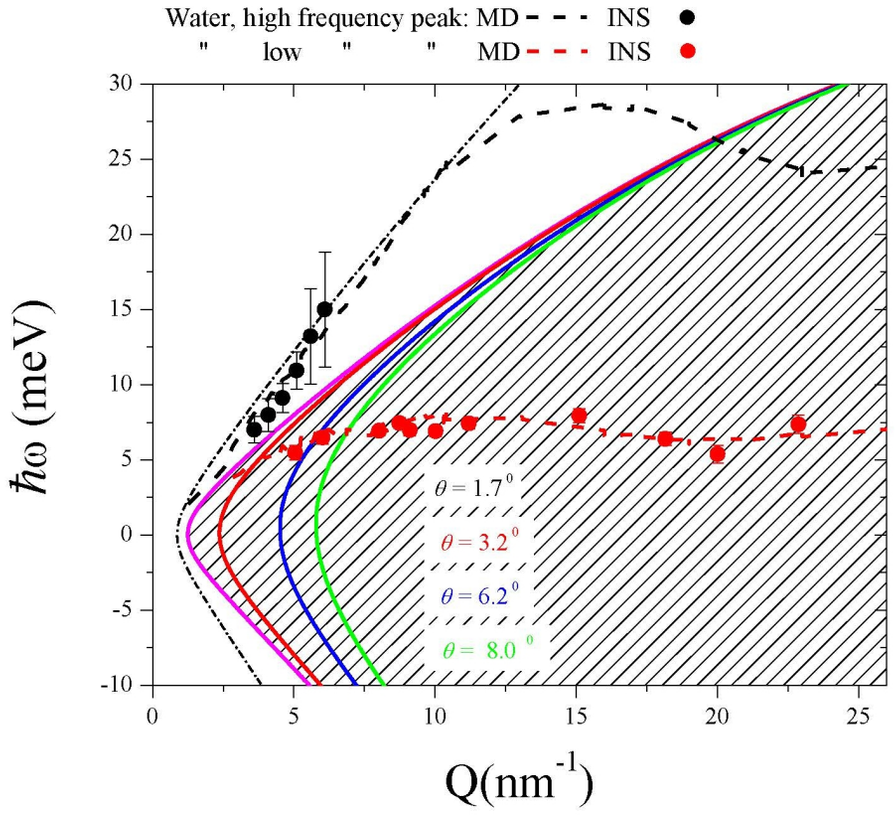

Figure 3. INS results in heavy water by [11] and [12] are reported as red and black dots, respectively, along with the MD simulation results of the two modes in the spectrum of water (dashed lines of corresponding color). The boundary of the explored dynamic region for the indicated scattering angle is reported with reference to the INS measurement by Bosi and coworkers. The shadowed area represents the dynamic domain accessible by such a measurement. The boundary of the dynamic plane explored by the Teixeira and coworkers' experiment is also indicated as a dot-dashed black line.

In particular, from the condition (2), it follows that, after the scattering event, the momentum of the photon $\hbar\vec{k}$ changes in direction, yet not in amplitude; therefore, one has:

$$Q^2 = k_I^2 + k_F^2 - 2k_I k_F \cos(2\theta) = 2k_I^2(1-\cos 2\theta) = \left(\frac{4\pi}{\lambda}\right)^2 \sin^2(\theta), \tag{37}$$

where $k_F = k_I = 2\pi/\lambda$, λ is the incident wavelength. The above formula shows that, for IXS, Q and ω are uncoupled, and, specifically, Q depends only on scattering angle and incident wavelength. This implies that the accessible portion of the dynamic plane is virtually unlimited at high (Q,ω) (virtual absence of kinematic limitations), while at small (Q,ω), it is still limited by the finite energy and momentum resolution of the spectrometer.

Taking advantage of the extension in the covered dynamic domain as well as of the statistical accuracy achievable with new synchrotron sources, recent IXS measurements on water droplets [13] evidenced a rather complex spectral shape. This contains both high and low

frequency inelastic modes, reminiscent of the sharper peaks dominating the phonon spectrum of ice, also measured in the same work. This clearly emerges from the two panels of Figure 4: the upper one, comparing the IXS measurement on a water droplet [13] to the INS one on heavy water [11] and lower one, which displays the IXS spectrum of ice.

It clearly appears that the superior spectral contrast of the INS measurement is the key to properly resolve the low energy mode, although this can only be achieved in a restricted dynamic range excluding all high frequency modes.

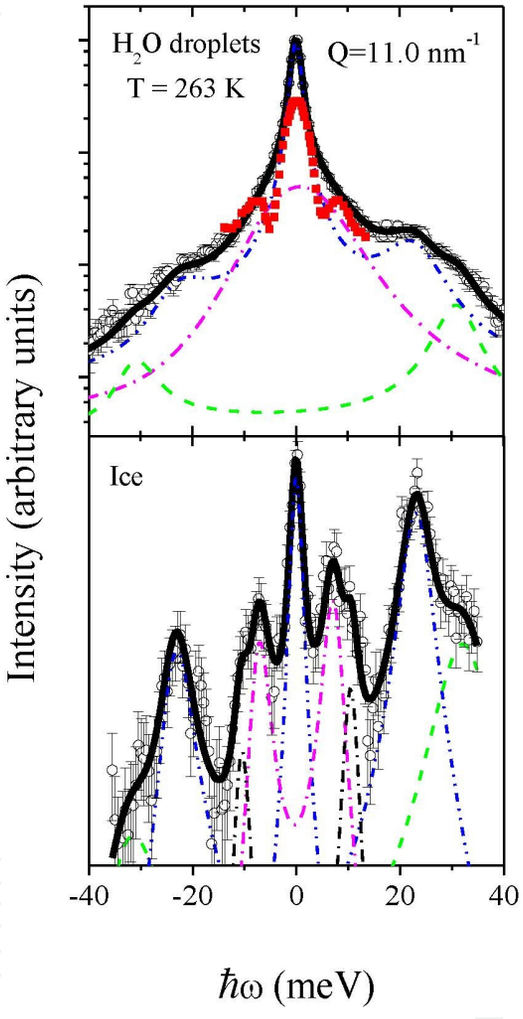

Figure 4. IXS spectra measured in a droplet of supercooled water (upper panel) and in ice (lower panel). Data are redrawn from [13] and are reported along with best fit line shape (thick black lines) and the various inelastic components (dotted lines). The INS spectrum of bulk heavy water at ambient temperature and same Q values is reported in the upper plot as redrawn from [11], after rescaling for an arbitrary intensity factor (red dots).

3.1.2. Constant Q scans

One of the major drawbacks of INS is that scans of E performed at constant θ in general do not provide a fixed-Q measurement, yet they change the Q value through Eq. 30. This E–Q coupling

http://dx.doi.org/10.5772/62844

is usually inconvenient because most theoretical models deal with constant Q (rather than constant θ) cuts of $S(Q,\omega)$. Two strategies are commonly used in INS experiments to measure constant Q spectra. The one firstly developed [1] is based on the use of triple axis spectrometers [14] in which θ and E movements can be coordinated to keep Q constant (through Eq. 30). This technique is rather time consuming since no more than one Q value can be measured in each scan. Conversely, time of flight (ToF) spectrometers [15] enable to map $S(Q,\omega)$ surfaces with points sparse in the (Q,ω) plane, which makes this technique much less time consuming. However, constant Q cuts of $S(Q,\omega)$ can only be interpolated using analytical models, yielding questionable results when $S(Q,\omega)$ surfaces are not sufficiently smooth.

3.1.3. Incoherent scattering

As discussed above, the incoherent scattering contribution to IXS intensity essentially arises from random fluctuations of the electronic form factor, $f(Q)$, while for INS it originates from fluctuations of the scattering length b. The latter depends on Z, A (the atomic number), and $\vec{J}$, the total (electron + nuclear) magnetic moment. The resulting scattering strength can thus be very different not only for different isotopes of the same material, but also for the same isotope species if these have total magnetic moment with different orientations. This can cause substantial mean square fluctuations of b, which provide a significant contribution to the incoherent part of the neutron cross section (indeed $\propto |\langle b\rangle|^2 - \langle |b|^2\rangle$). Obviously, this is a serious drawback if the experiment aims at investigating the collective dynamics of the sample, as for the examples discussed in this chapter. However, it represents a valuable resource when the experiment focuses on single molecule's dynamics of, because the incoherent scattering provides direct insight on it. In this respect, highly hydrogenated systems are ideal sample for incoherent INS measurements, owing to almost fully incoherent character of the INS cross section of hydrogen.

3.1.4. Incident flux on the sample

Although IXS can be considered a "photon hungry" technique, state of art IXS spectrometers have incident fluxes much higher than that their INS counterparts. Typically, IXS beamlines can produce a photon flux of 10^9–10^{10} photons/s within a focal spot as narrow as 100 μm^2, while for ToF spectrometers, a flux of ≈10^5 photons/s is typically achieved within focal spot of a few square centimeters. Although the collection/spectral analysis of IXS spectrometers ultimately imposes severe intensity penalties, mostly due to the relatively low angular acceptance of IXS analyzers, the final count rate of meV-resolution IXS measurements is usually much higher than that of their INS counterparts.

3.1.5. Multiple scattering

As mentioned, the leading contribution to the attenuation of IXS signal is the photoelectric absorption, which, on the bright side, also causes a strong suppression of multiple scattering events. As a consequence, in IXS measurements the multiple scattering intensity is often negligible compared to the single scattering signal, which is the one proportional to $S(Q,\omega)$. The situation is radically different for INS measurements, for which the attenuation is

dominated by the scattering process itself, and, therefore, multiple scattering events substantially contribute to the inelastic signal.

3.1.6. Transverse beam size

The incident beam of typical IXS spectrometers has an extremely small focal spot, usually few tens of square micrometer or even less. This permits IXS experiments to deal with small-sized samples, thus potentially disclosing the access to extreme thermodynamic conditions, such as high pressure and extremely low or high temperature. This is also a valuable asset when dealing with samples only available in small volumes. The use of smaller samples in IXS measurements is also fostered by the usually high absorption, especially for high Z materials. Conversely, the neutron beam is much larger in size and, also, more deeply penetrating inside the matter and this makes small samples relatively "transparent" to this technique.

3.2. Part B: advantages of INS

3.2.1. Resolution shape

Probably, the most important advantage of INS over IXS is the narrower and sharper energy resolution function. Most importantly, INS offers the opportunity of tailoring the energy resolution width .In fact, the latter can be narrowed according to the specific needs of experimenters, although, unavoidably, to the cost of a shrinkage of the dynamic range covered. The use of a narrow and sharp resolution is crucial in many applications including, for instance, the study of the slow dynamic response of highly viscous systems as glass formers approaching the melting. In fact, in this case all relevant spectral features concentrate in the so-called quasi-elastic region of the spectrum. Resolution functions as narrow as a few meV can be reached using cold neutrons as a probe. Furthermore, INS resolution profiles are usually sharp (nearly Gaussian) as opposite to the broad (mostly Lorentzian) IXS resolution wings.

Although new concept IXS spectrometers discussed in the following promise a drastic improvement of both resolution width (sub-meV) and spectral contrast, the performance of quasi-elastic neutron scattering instruments [16] is unlikely to be ever matched by IXS spectrometers.

3.2.2. Q-decay of the cross section

Due to the highly localized interaction of neutrons with the target nuclei, no appreciable Q decay of the scattering length can be observed up to Q values of the order of the inverse of the nuclear size. This value is nearly a factor 10^3 larger than the typical Q value at which the IXS cross halves its $Q = 0$ value. For this reason, the use of neutrons is particularly convenient for extremely high Q measurements probing the so-called single particle, or impulse approximation, regime [17]. Indeed, the access to this regime has been an exclusive task of deep inelastic neutron scattering (DINS) for decades ([18]. Although some successful attempts to reach the impulse approximation with IXS have been reported in the literature [19], the maximum Q

http://dx.doi.org/10.5772/62844

reached by these measurements is still smaller than the range covered by DINS for more than two orders of magnitude.

3.2.3. Absorption

As mentioned, at the typical incident energies of IXS, the scattered intensity is mostly attenuated by the photoelectric absorption, whose coefficient μ is proportional to Z^4. In high Z samples the absorption dominates over the Thomson scattering term, thus making IXS of limited efficiency for these materials. Conversely, the neutron absorption cross section is, in most cases, relatively low, which makes neutrons an ideal, non-destructive, probe of bulk properties of materials. The low absorption is also a crucial pre-requisite to probe biological systems because a low incident flux reduces the risk of radiation-induced damage in these samples [20]. Consequently, complex or delicate biological materials can be studied less destructively than any other forms of high energy radiation. Even in vivo studies are now being carried out using neutron probes, an area that has great potential for further development and applications in medical research.

On the other hand, the larger penetration depth of neutron probes comes in handy in some large volume high-pressure applications, as it makes the design of high-pressure vessels more straightforward. In fact the cell body can be often penetrated by the neutron beam with no need of using neutron-transparent windows, thereby drastically reducing the risk of high-pressure leaks.

3.2.4. Single particle dynamics

The neutron cross section of hydrogen is substantially higher than the one of other atomic species and is almost completely incoherent. This represents a key advantage when studying the single particle response of hydrogen compounds as well as hydration patterns in proteins and other macromolecules [21].

3.2.5. Contrast variation

When the sample is embedded or floating in a substrate, as for confined systems, solutions, and so on, it is often useful to improve the contrast of the measurement, i.e. the difference between the scattering intensity from the confined sample and the one from the substrate. In principle, the contrast can be enhanced by manipulating the scattering density of a specific component.

However, the IXS intensity of a given component can only be manipulated changing the atomic number, i.e. altering the chemical species. Conversely, the neutron scattering cross section is isotope-specific. Therefore, the scattering can be substantially manipulated through the change of the isotopic composition in the sample, i.e. without altering its chemical properties. This suggests to modulate the cross section by means of a mere isotopic substitution to optimize the contrast [22].

3.2.6. Isotopic substitution

As discussed just above, the INS cross section is isotope-specific, i.e. it depends on the nuclear mass, but not on the atomic number, or, equivalently, the chemical specie of the target sample. One method taking full advantage of this property is based upon parallel INS measurements on chemically equivalent systems in which an "isotopic substitution" has been implemented. In fact, by using a smart isotope manipulation, one in principle can selectively enhance the partial scattering contribution of different atomic species in a molecular sample, or in a mixture [22].

4. Present and future of IXS: ID28 beamline at ESRF and 10ID beamline at NSLS II

4.1. An example of state-of-art IXS spectrometer: ID28 beamline

As discussed in the introductory section, the investigation of collective modes in the spectrum of density fluctuations of fluids imposes a challenging requirement on the relative energy resolution ($\Delta E/E \leq 10^{-7}$). The implementation of IXS monochromators with the required $\Delta E/E$ demands the use of extremely high quality crystals, i.e. crystals having a relative lattice parameter variation, $\Delta d/d$, smaller than 10^{-7}, at least within their active part (diffracting volume).

Furthermore, to preserve the desired energy resolution without significantly reducing the photon flux, the whole divergence of the incoming photon beam must fall within the intrinsic angular acceptance of the considered monochromator reflection, i.e. the Darwin width, w_{D}. Within the dynamical theory of X-ray diffraction [23], the latter is given by:

$$w_D = (AE / E)h \tan\theta_B,$$

where h and θ_B are the Bragg reflection order and angle, respectively. Since $\tan\theta_B$ diverges for $\theta_B \approx 90°$, upon approaching a backscattering geometry w_D can be enhanced enough to accept the X-ray beams delivered by standard undulators' sources.

Therefore, it was predicted almost 50 years ago that the use of extreme backscattering geometries coupled with the small $\Delta E/E$ typical of high order (high h) Bragg reflections could in principle enable high-resolution (meV) IXS measurements. Historically, the first demonstration that the needed 10^{-7} relative resolution can be achieved with silicon crystals in backscattering geometry was given by [24] and [25]; these results were further developed by [26] for applications to IXS.

The $\Delta E/E$ ultimately achieved in these works was 5×10^{-7} with a photon flux of ~10^6 photons/s on the sample. However, the best performance achieved back at those times ($\Delta E/E \approx 3.5 \times 10^{-7}$ within 2.1 μrad angular acceptance) exploited a "four bounce" crystal array, originally developed for resonant nuclear scattering with synchrotron radiation [27].

http://dx.doi.org/10.5772/62844

The first complete meV-resolution IXS spectrometer, ID16 beamline, was built on 1995 at the European Synchrotron Radiation Facility (ESRF) in Grenoble, France. Few years later another IXS spectrometer, ID28 beamline [31], was developed at *ESRF* with a similar design, yet enabling an extended Q-range coverage. This is the only meV-resolution spectrometer currently active at ESRF and its general description is concisely reported in the following. It is worth stressing, that other meV-resolution IXS spectrometers with slightly different layouts are currently available in Japan [32] and United States [33, 34].

As evident from Figure 5, the design of ID28 (and all current IXS spectrometers) is based on the triple axis concept, first developed in the mid-1950s [1]: the first axis locates at the monochromator crystal, and rotations around it are used to select the energy of incident photons. Rotations around the second axis, located at the sample position, change instead the momentum transfer $\vec{Q}$. Finally, the third axis is the one of the analyzer crystals, and, in principle, rotations around it determine the energy scattered photons, $\hbar\omega_f$. A more detailed layout and a picture of ID28 beamline can be found in Figures 6 and 7, respectively.

At variance of traditional triple axis schemes, implementing energy scans of scattered intensity through rotations of the analyzer crystal(s), at ID28 beamline, these are performed by changing the *d*-spacing of reflecting crystals through the scan of their temperature. The achievement of a $10^{-7} \div 10^{-8}$ relative energy resolution demands a millikelvin accuracy in the temperature control of the monochromator/analyzer optics. This is obtained by using a carefully designed temperature bath controlled by an active feedback system with a precision of 0.2 mK at ambient conditions.

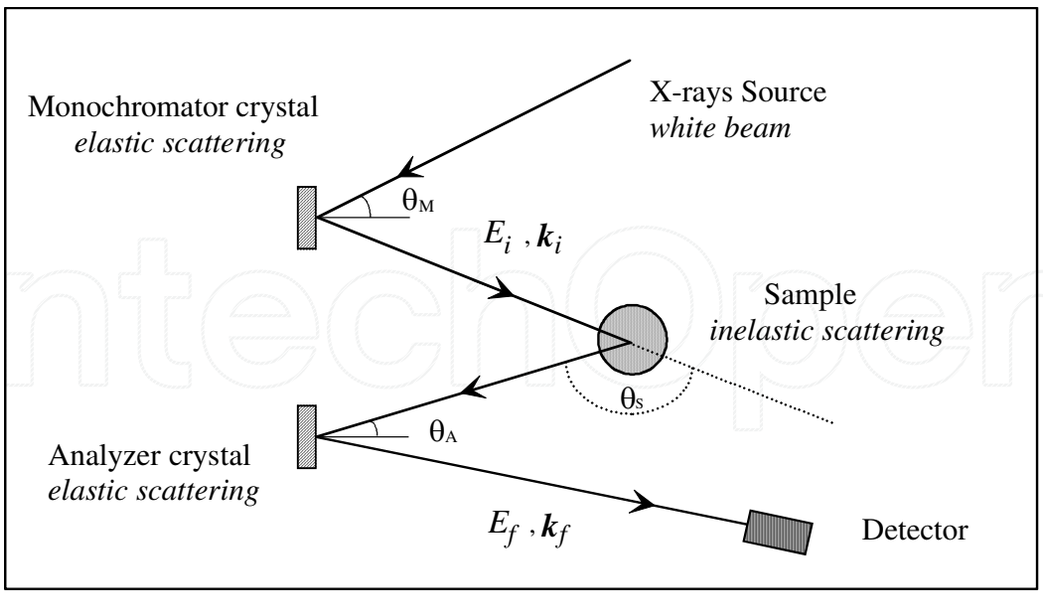

Figure 5. The general scheme of the ID28 IXS spectrometer at ESRF.

The X-ray source consists of three undulators having 32 mm magnetic period, placed in a straight high-beta β section of the electron storage ring. The utilized X-ray radiation energies

correspond to the undulator emission of the third or fifth harmonic. The X-ray beam delivered at these harmonics has $\Delta E/E \approx 10^{-2}$, a 40×15 μRad (horizontal × vertical) angular divergence and about 200 W integrated power. Such a beam is pre-monochromatized to $\Delta E / E \approx 2 \times 10^{-4}$ $\Delta E / E \approx 2 \cdot 10^{-4}$ using a silicon, Si(1,1,1), in vacuum and cryogenically cooled channel-cut crystal. Its main task is to absorb the relevant portion of the irradiated power that will be otherwise impinging on the main monochromator, thus drastically reducing its heat load. This is required to minimize thermal deformations induced on the monochromator crystal that can drastically degrade the energy resolution. The x-photon beam filtered by the pre-monochromator is then back reflected by the high-resolution monochromator, consisting of an asymmetrically cut silicon crystal oriented along the [111] direction and operated at a Bragg angle of 89.98°. This extreme backscattering geometry minimizes geometrical contributions to the total energy resolution broadening. Under these conditions, the angular acceptance of the monochromator is larger than the X-ray beam divergence and all photons are thus reflected within the desired energy bandwidth. Both the use of high-order Bragg reflections (h,h,h) with $(h = 7,8,9,11,12,13)$ and the superior quality of the active optics are required to ultimately achieve the needed relative resolution $\Delta E / E \approx 10^{-7} \div 10^{-8}$. The monochromatic beam is focused on the horizontal and vertical planes by a platinum-coated toroidal mirror, located 25 m upstream of the sample, which provides a $250 \times 80\ \mu m^2$ full width at half maximum (FWHM). More performing optical elements are also available at ID28 to focus the beam down to 30 × 40 μm².

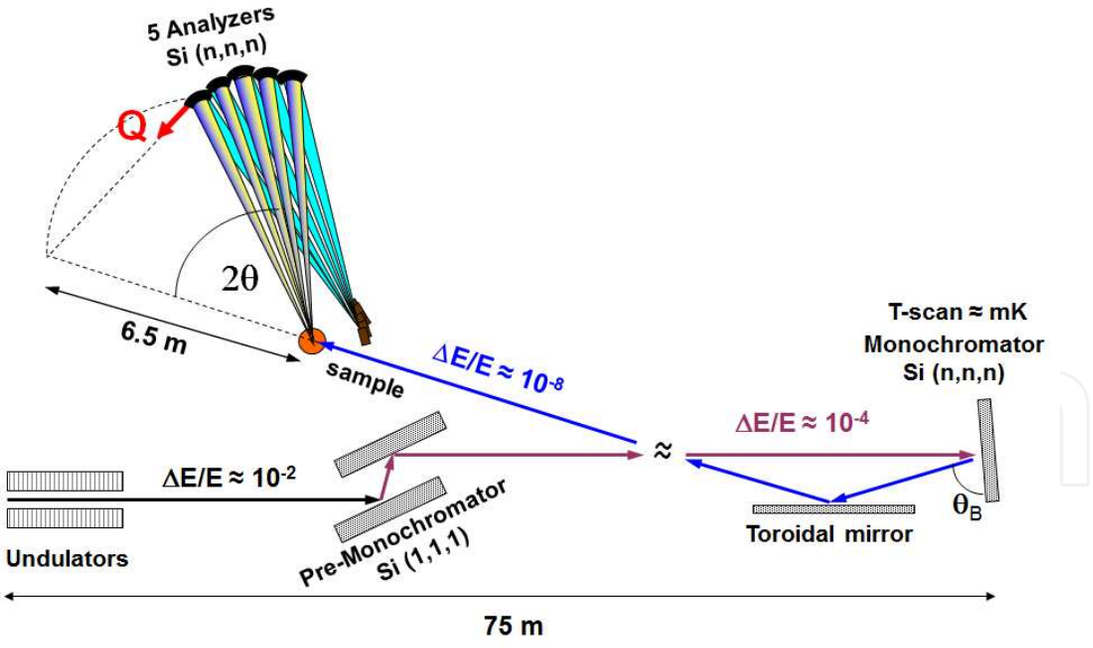

Figure 6. The schematic layout of ID28 beamline at ESRF (courtesy of F. Bencivenga).

The energy of the radiation scattered by the sample is analyzed by five spherical analyzers (nine in the upgraded instrument) mounted on the tip of an horizontal arm, which can be rotated by an angle 2θ so as to reach the desired exchanged momentum. These five (nine)

http://dx.doi.org/10.5772/62844

analyzer units have a mutual angular offset, which enables the simultaneous collection of IXS spectra at five (nine) different *Q*s. Although the problems connected to the energy resolution are conceptually the same for monochromator and analyzer, the required angular acceptance is very different in the two cases. For the analyzer, the optimal angular acceptance results from the best compromise between conflicting count rate and Q-resolution requirements. In fact, albeit a reduction of the angular acceptance improves the momentum resolution, it reduces the overall count rate.

Figure 7. The ID28 beamline's spectrometer arm of at ESRF (from the ID28 beamline's website, courtesy of A. Bosak)

Considering that for typical IXS measurements an acceptable Q spread is, at the lowest Q's, $\Delta Q_{\mathrm{M}} \leq 0.1 \div 0.5\ \mathrm{nm}^{-1}\ 0.1 \div 0.5\ nm^{-1}$, the angular acceptance of the analyzer is correspondingly set to few milliradians, a value much larger than the Darwin width of the Bragg reflections typically used. The only option to achieve such a large acceptance is the design of a focusing system, which, however, must minimize possible distortions of the *d*-spacing ultimately degrading the energy resolution. The solution actually adopted at ID28 beamline is a mosaic of ≈12,000 silicon perfect single square crystals glued on a spherical surface. These analyzer arrays are operated in a 1:1 pseudo-Rowland circle geometry with aberration low enough not to degrade appreciably the desired energy resolution [28].

Each analyzer is equipped with motorized entrance slits setting the desired Q-resolution, its back-reflection being intercepted by Peltier-cooled silicon diode with extremely low dark count (≈1 count over 30 minutes).

The spectrometer arm can be rotated around a vertical axis passing through the sample by an < 55°, which corresponds to Q < 100 nm^{-1}, for Si(11,11,11) monochromator/analyzer Bragg reflection.

The measured resolution profile of the instrument has a FWHM of approximately 1.5 meV, as required to perform spectroscopy measurements of the high frequency dynamics of disordered systems.

4.2. Toward a new generation IXS spectrometer

On a general ground, high resolution measurements as the one discussed above suffer from major drawbacks: the relatively large width of the resolution (≥1 meV) and, perhaps more importantly, the poor spectral contrast, i.e. the slowly decaying (essentially Lorentzian) wings of the instrumental resolution profile. The development of next generation IXS instruments using a new monochromatization/energy analysis holds the promise of effectively tackling these problems.

Currently, state-of-art IXS spectrometers have a working principle similar to the one of the ID28 beamline of ESRF illustrated above, i.e. they use extreme backscattering geometries in which the energy analysis is implemented through temperature scans [28].

In these schemes, the final achievement of a meV-resolution resolution is challenged by two major difficulties: (1) the energy analysis imposes tight constraints on the temperature stability of the optics, as only $<10^{-4}$ K temperature gradients can be tolerated and (2) the higher order Bragg reflections are more deeply penetrating into reflecting crystals, thus being severely affected by extinction losses.

A few alternative schemes based on the dispersion character of Bragg back reflection from asymmetrically cut crystals [35] have been successfully tested. Namely:

1. an array of four silicon crystals, customarily referred to as 4-bounce monochromator [36] and
2. an assembly of collimator (*C*), dispersive (*D*), and wavelength (*W*) selector crystals, usually referred to as *CDW*, or *CDDW*, if two dispersive crystals are used instead [37].

Both optical schemes demonstrated to provide sub-meV broad and extremely sharp, essentially Gaussian, resolution profiles. Furthermore, these optical schemes have a wealth of advantages when compared to current backscattering IXS spectrometers:

1. They do not use high order Bragg reflections, which greatly improves their overall efficiency. In fact, they are operated at moderate energy values at which synchrotron undulators usually perform best.
2. The spectral contrast, i.e. the sharpness of the resolution function, is greatly enhanced by the multiple reflection bounces.

http://dx.doi.org/10.5772/62844

3. They are extremely flexible, offering the opportunity of changing incident energy and tailoring the resolution to any specific needs.

The feasibility of these schemes for IXS application was recently demonstrated [38]. Most importantly, a novel instrument (10ID beamline) with a very narrow (sub-meV) and sharp (essentially Gaussian) resolution function [39, 40] will be soon operated at the new synchrotron source NSLS-II in Upton, New York. A schematic representation of the various components of such a beamline is provided in Figure 8.

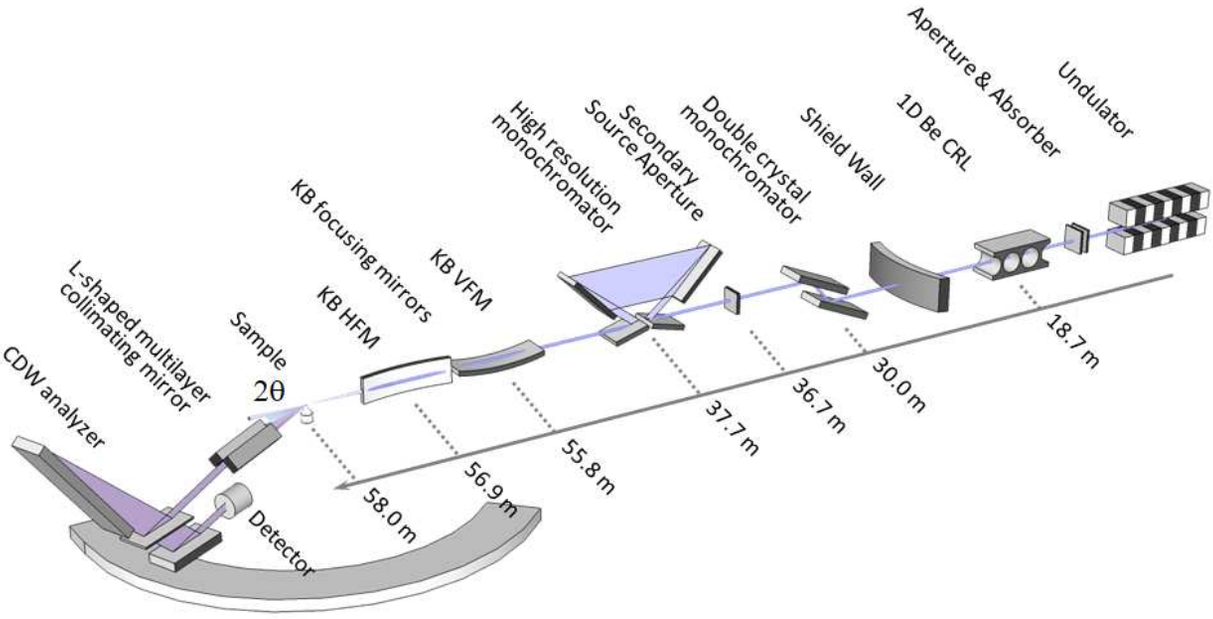

Figure 8. A schematic layout of the new high resolution IXS spectrometer soon available at NSLS II, taken from [40].

5. An example of a joint IXS and IXS experiment: the study of a shear mode propagation in water

Among various topics emerging from the vast literature on THz measurements of S(Q,ω) of liquids, one of the most controversial focuses on the presence of a second, low frequency, mode in the spectrum of water. More than other research subjects, this topic lends itself to the synergic use of the two complementary THz spectroscopic methods discussed above: IXS and INS.

As mentioned, the presence of the the low-frequency peak of water was also reported in the INS work of [11] and in the later INS measurement by [41]. Both these works, owing to the mentioned kinematic limitations, could not access to the high frequency back then referred, somehow misleadingly (see [42, 43]), to as the "fast sound mode", which was instead observed in the INS work of Teixeira and coworkers [12]. For a long time, the low frequency mode was interpreted as the finite-Q extension of the macroscopic sound mode, based on the overall

consistency between the slope of its low Q dispersion curve and the known value of the adiabatic sound speed [44]. This interpretation was confuted years later by both MD [10] and IXS [45] studies of the water spectrum, which demonstrated that such low frequency mode has instead a transverse acoustic origin. This interpretation initially raised some controversy [46, 47], but found important validations in successive IXS works [13, 45]; a concise account of these studies can be found in [48].

In a way, the onset of a transverse mode in the spectrum of a disorder material may not be too surprising as one recognizes that quasi-polarized (transverse or longitudinal) modes are routinely observed in the inelastic spectra of poly-crystals in the first-Brillouin zone. Therefore, the hypothesis that a definite polarization, either longitudinal or transverse, are intertwined has in principle some ground for a liquid system, especially over distances matching the size of molecular disorder. However, it is broadly accepted that a longitudinal or transverse polarization can be still assigned to a mode in the mesoscopic regime, provided such a mode dominates the current spectra of corresponding – longitudinal or transverse – polarization. Longitudinal current spectra $C_L(Q,\omega)$ are directly determined from the experimentally measured $S(Q,\omega)$ using $C_L(Q,\omega) = (\omega/Q)^2 S(Q,\omega)$. Conversely, transverse current spectra $C_L(Q,\omega)$ can only be determined by computer simulations as the Fourier transform of the autocorrelation function between transverse components of atomic velocities.

It is worth recalling that the (transverse or longitudinal) polarization of the acoustic mode is defined in reference to the direction of the exchanged momentum $\hbar\vec{Q}$. In this respect, it is useful to recall that $S(Q,\omega)$ is the Fourier transform of the correlation function $\sum_{jk}\langle \exp[i\vec{Q}\cdot\vec{R}_k(t)]\exp[i\vec{Q}\cdot\vec{R}_k(t)]\rangle$. Clearly, the presence of the $\vec{Q}\cdot\vec{R}_i(t)$ term in the exponents shows that only longitudinal movements, i.e. movements along the $\vec{Q}$ direction, are relevant to $S(Q,\omega)$. Transverse modes are therefore visible in the $S(Q,\omega)$ shape only indirectly, via the so-called longitudinal–transverse (L–T) coupling. This mainly consists in a coupling between transverse and longitudinal waves, which occurs above some Q threshold. For instance, in water, this threshold was located at 4 or ≈6 nm^{-1} by [49] and [50], respectively.

The onset of an L–T coupling in liquids has been often associated to the intrinsically "open" (large free volume) tetrahedral structure of water, as opposite to the essentially close-packed arrangement of "normal" fluids. In fact, an L–T coupling has been observed in tetrahedral systems such as water itself as well as GeO_2 [52] and $GeSe_2$ [53].

However, nowadays, this interpretation needs some reconsideration because the L–T coupling was also observed in non-tetrahedral systems, such as glassy glycerol [54] and liquid metals [55-59]. Furthermore, a similar effect was reported in more complex systems such as binary mixtures [51] and biophysical samples [60-62].

On a general ground, the ability to support shear propagation can be considered as a manifestation of the solid-like response of a fluid at short times and distances. This seems consistent to the early IXS work of [49], where substantial similarities between the THz dynamic response of water and ice were suggested. Also, based on previous lattice vibrations, i.e. calculations and INS measurements [64], this additional spectral feature in water was assigned to the transverse optical (TO) visible in ice. Consistently with this scenario, the IXS work of Ponte-

corvo and coworkers [45] also demonstrated that an L–T coupling is only visible when density fluctuations propagate at frequencies larger than the inverse of the relaxation time $1/\tau$. Under these conditions, acoustic waves "perceive" the propagation medium as frozen as expected for a glass. These slows degrees of freedom cannot energetically couple with the acoustic wave, which, therefore, travel "elastically," that is keeping its energy constant. The virtual lack of acoustic dissipation of this elastic regime is reflected by the higher sound velocity and the lower sound damping. Furthermore, restoring forces become more effective in fostering a sound propagation in the shear plane. This seems consistent with the result of a successive IXS work [13], where a study of shear mode propagation was jointly performed in normal liquid, solid, and supercooled phase of water.

5.1. The joint use of IXS and INS

The various IXS investigations of transverse propagation in water mentioned above often pushed to limit the capability of this spectroscopic method; as a matter of fact, these studies could be successfully accomplished either reaching somehow extreme thermodynamic conditions (high density and/or low temperature) or accessing to large Q values.

The observation of a transverse mode at low Q's or at high T's would have required a sharp and narrow resolution function, definitely beyond the current capability of IXS. In principle, INS measurements can offer the required resolution performance, but only by confining the covered dynamic range within a restricted region excluding the longitudinal, high frequency, mode (see data reported in Figure 3). A possible method to circumvent these complementary limitations foresees simultaneous IXS and INS measurements on the same heavy water sample.

This is the strategy followed by joint INS–IXS measurement in heavy water [50] and in a successive one on deuterated water–glycerol mixtures [51]. The use of deuterated samples was, of course, imposed by the highly incoherent INS cross section of hydrogen, which would have prevented the INS measurement to reliably determine the coherent spectrum. In these two measurements, the INS spectrometer was operated using an extremely narrow (<0.1 meV) and essentially Gaussian resolution profile, as required for an optimal characterization of the low frequency portion of the spectrum. The parallel use of IXS allowed to dramatically extending the low energy range covered by the neutron experiment. Figure 9 provides an example of spectra measured in heavy water by these two complementary techniques.

Consistent to the other works in the literature [65], the spectrum was approximated by a viscoelastic model accounting for the longitudinal component of density fluctuations, while the additional peak in the spectrum generated by the L–T coupling was approximated by a simple Damped Harmonic Oscillator (DHO) term [66]:

$$\frac{S(Q,\omega)}{S(Q)} = (1-\tilde{T})S_{\mathrm{VE}}(Q,\omega) + \tilde{T}\frac{1}{\pi}\frac{2\Omega_t^2\Gamma_t}{\left[\omega^2-\Omega_t^2\right]^2+4\Gamma_t^2\omega^2}, \tag{38}$$

where the suffix "VE" labels the viscoelastic model, while Ω_t and Γ_t represent, respectively, the characteristic frequency and damping of the low-frequency excitation. Finally, $\tilde{T}$ is a Q-

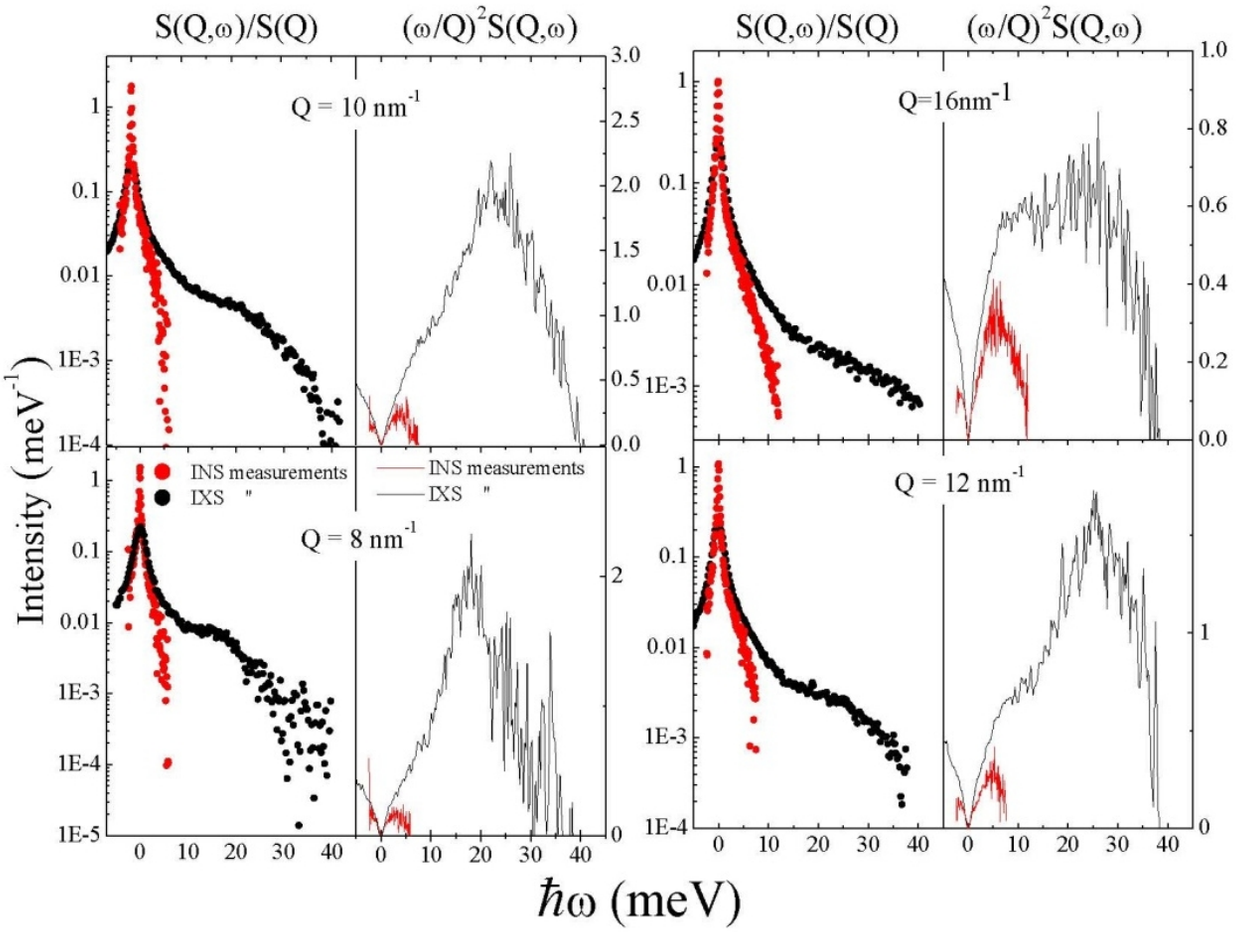

Figure 9. Representative IXS (black dots) and INS (black dots) measurements of water spectra are reported along with the corresponding current spectra (lines of corresponding color). All reported curves are normalized to the S(Q) for consistency. Data are redrawn with permission from Ref. [51], which is copyrighted by the American Physical Society.

dependent scaling factor, yielding the relative weight of the DHO component. Within the hypothesis that the DHO term arises from the L–T coupling, $\widetilde{T}$ provides a measure of the strength of such coupling. An important outcome of this joint measurement is reported in Figure 10.

It clearly appears that at low Q, the transverse mode becomes heavily damped, being its frequency nearly equal to the damping, and therefore, the transverse perturbation assumes a essentially non-propagating character. Interestingly, when this low Q regime is reached, both acoustic frequency and damping are of the same order and the elastic (solid-like) character of the dynamics is lost. At even lower Q values, no clear evidence of a transverse mode in the spectrum can be inferred from measured spectral shape.

The trend discussed above indicates that below the Q threshold of the L–T mode, the inelastic peak merges into the quasi-elastic mode typical of all fluids exhibiting a viscoelastic behavior. This is the well-known Mountain [67] mode, which arises from the coupling of density fluctuations with active relaxation processes.

http://dx.doi.org/10.5772/62844

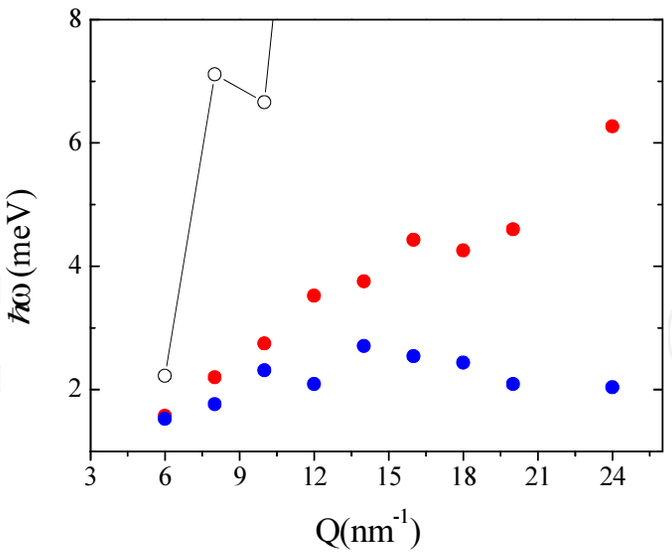

Figure 10. The Q dependence of the frequency Ω_t (red dots) and the damping Γ_t (blue dots) of the transverse acoustic mode in water spectrum are reported along with the inverse of the relaxation time (open circles + line). Data are re-drawn with permission from Ref. [51], which is copyrighted by the American Physical Society.

Acknowledgements

The work performed at National Synchrotron Light Source II, Brookhaven National Laboratory, was supported by the U.S. Department of Energy, Office of Science, Office of Basic Energy Sciences, under Contract No. DE-SC0012704.

Author details

Alessandro Cunsolo

Address all correspondence to: acunsolo@bnl.gov

National Synchrotron Light Source II, Brookhaven National Laboratory, Upton, NY, USA

References

[1] Brockhouse BN, Stewart AT. Scattering of neutrons by phonons in an aluminum single crystal. Phys. Rev. 1955; 100:756-757. DOI: http://dx.doi.org/10.1103/PhysRev.100.756

[2] Goodman JW. Introduction to Fourier optics. 3rd ed. Grenwood Village: Roberts and Company Publishers; 2005.

[3] Jackson JD, Jackson JD. Classical electrodynamics. Vol. 3. New York: Wiley, 1962.

[4] Sinha SK. Theory of inelastic x-ray scattering from condensed matter. J. Phys. Condens. Matter 2001, 13:7511-7523. DOI: http://dx.doi.org/10.1088/0953-8984/13/34/304

[5] Dirac PA. The quantum theory of the emission and absorption of radiation. Proc. R. Soc. A, 1927, 40:243-265.

[6] Van Hove L. Correlations in space and time and born approximation scattering in systems of interacting particles. Phys. Rev. 1954, 95:249-262. DOI: http://dx.doi.org/10.1103/PhysRev.95.249

[7] Schulke W. Inelastic scattering by electronic excitations. In: Brown G, Moncton DE, editors. Handbook on synchrotron radiation, Amsterdam:Elsevier, 1991; Vol. 3.

[8] Lovesey SW. Theory of neutron scattering from condensed matter. Oxford: Clarendon Press, 1984; Vol. 1.

[9] Rahman A, Stillinger FH. Propagation of sound in water. A molecular-dynamics study. Phys. Rev. A 1974, 10:368-378. DOI: http://dx.doi.org/10.1103/PhysRevA.10.368

[10] Sampoli M, Ruocco G, Sette F. Mixing of longitudinal and transverse dynamics in liquid water. Phys. Rev. Lett. 1997, 79:1678-1681. DOI: http://dx.doi.org/10.1103/PhysRevLett.79.1678

[11] Bosi P, Dupré F, Menzinger F, Sacchetti F, Spinelli MC. Observation of collective excitations in heavy-water in 108 cm-1 momentum range. Nuovo Cimento Lett. 1978, 21:436-440. DOI: 10.1007/BF02763195

[12] Teixeira J, Bellissent-Funel MC, Chen SH, Dorner B. Observation of new short wavelength collective excitations in heavy water by coherent inelastic neutron scattering. Phys. Rev. Lett. 1985, 54:2681-2683. DOI: http://dx.doi.org/10.1103/PhysRevLett.54.2681

[13] Cimatoribus A, Saccani S, Bencivenga F, Gessini A, Izzo MG, Masciovecchio C. The mixed longitudinal-transverse nature of collective modes in water. New J. Phys. 2010, 12: 053008. DOI: http://dx.doi.org/10.1088/1367-2630/12/5/053008

[14] Shirane G, Shapiro SM, Tranquada JM. Neutron scattering with a triple-axis spectrometer: Basic techniques. Cambridge: Cambridge University Press, 2002.

[15] Windsor CG. Pulsed neutron scattering. London:Taylor & Francis, 1981.

[16] Bée M. Quasielastic neutron scattering : Principles and applications in solid state chemistry, biology and materials science. Bristol: Hilger, 1988.

[17] Silver RN, Sokol PE. Momentum distributions. New York: Springer Science+ Business Media, 2013.

[18] Sears VF. Scaling and final-state interactions in deep-inelastic neutron scattering. Phys. Rev. B 1984, 30:44-51. DOI: http://dx.doi.org/10.1103/PhysRevB.30.44

[19] Monaco G, Cunsolo A, Pratesi G, Sette F, Verbeni R. Deep inelastic atomic scattering of X rays in liquid neon. Phys. Rev. Lett. 2002, 88:227401. DOI: http://dx.doi.org/10.1103/PhysRevLett.88.227401

[20] Rheinstadter MC, Ollinger C, Fragneto G, Demmel F, Salditt T. Collective dynamics of lipid membranes studied by inelastic neutron scattering. Phys. Rev. Lett. 2004, 93:108107. DOI: http://dx.doi.org/10.1103/PhysRevLett.88.227401

[21] Middendorf HD. Biophysical applications of quasi-elastic and inelastic neutron scattering. Annu. Rev. Biophys. Bioeng. 1984, 13:425-451. DOI: 10.1146/annurev.bb.13.060184.002233

[22] Finney J, Soper A. Solvent structure and perturbations in solutions of chemical and biological importance. Chem. Soc. Rev. 1994, 23:1-10. DOI: 10.1039/CS9942300001

[23] Zachariasen W. A general theory of x-ray diffraction in crystals. Acta Cryst. 1967, 23:558-564. DOI: 10.1107/S0365110X670032

[24] Ando M, Bailey D, Hart M. A simple Bragg-spacing comparator. Acta Cryst. A 1978, 34:484-489. DOI: 10.1107/S0567739478001047

[25] Graeff W, Materlik G. Millielectron volt energy resolution in Bragg backscattering. Nucl. Inst. Meth. 1982, 195:97-103. DOI: 10.1016/0029-554X(82)90764-9

[26] Dorner B, Burkel E, Peisl J. An x-ray backscattering instrument with very-high-energy resolution. Nucl. Inst. Meth. A 1986, 246:450-451. DOI: 10.1016/0168-9002(86)90130-0

[27] Faigel G, Siddons DP, Hastings JB, Haustein PE, Grover JR, Remeika JP, Cooper AS. New approach to the study of nuclear Bragg scattering of synchrotron radiation. Phys. Rev. Lett. 1987, 58:2699-2701. DOI: http://dx.doi.org/10.1103/PhysRevLett.58.2699

[28] Masciovecchio C, Bergmann U, Krisch M, Ruocco G, Sette F, Verbeni R. A. Perfect crystal x-ray analyser with 1.5 meV energy resolution. Nucl. Inst. Meth. B 1996, 117:339-340. DOI: 10.1016/0168-583X(96)00334-5

[29] Verbeni R, Sette F, Krisch MH, Bergmann U, Gorges B, Halcoussis C, Martel K, Masciovecchio C, Ribois JF, Ruocco G, Sinn H. X-ray monochromator with 2 x108 energy resolution. J. Synchrotron Radiat. 1996, 3:62-64. DOI: 10.1107/S0909049595015883

[30] Sette F, Ruocco G, Krisch M, Bergmann U, Masciovecchio C, Mazzacurati V, Signorelli G, Verbeni R. Collective dynamics in water by high energy resolution inelastic x-ray scattering. Phys. Rev. Lett. 1995, 75:850-853. DOI: http://dx.doi.org/10.1103/PhysRevLett.75.850

[31] Krisch M. Status of phonon studies at high pressure by inelastic x-ray scattering. J. Raman Spectrosc. 2003, 34:628-632. DOI: 10.1002/jrs.1033

[32] Baron AQR, Tanaka Y, Miwa D, Ishikawa D, Mochizuki T, Takeshita K. Goto S, Matsushita T, Kimura H, Yamamoto F, Ishikawa T. Early commissioning of the Spring-8 beamline for high resolution inelastic X-ray scattering. Nucl. Inst. Meth. A 2001, 467:627-630. DOI: 10.1016/S0168-9002(01)00431-4

[33] Toellner TS, Alatas A, Said AH. Six-reflection mev-monochromator for synchrotron radiation. J. Synchrotron Radiat. 2011, 18:605-611. DOI: 10.1107/S0909049511017535

[34] Said AH, Sinn H, Divan R. New developments in fabrication of high-energy-resolution analyzers for inelastic x-ray spectroscopy. J. Synchrotron Radiat. 2011, 18:492-496. DOI: 10.1107/S0909049511001828

[35] Shvyd'ko Y. X-ray optics—high-energy-resolution applications, optical science. Berlin:Springer, 2004; Vol. 98.

[36] Yabashi M, Tamasaku K, Kikuta S, Ishikawa T. X-ray monochromator with an energy resolution of 8×10−9 at 14.41 kev. Rev. Sci. Inst. 2001, 72:4080-4083. DOI: http://dx.doi.org/10.1063/1.1406925

[37] Shvyd'ko YV, Lerche M, Kuetgens U, Ruter HD, Alatas A, Zhao J. X-ray Bragg diffraction in asymmetric backscattering geometry. Phys. Rev. Lett. 2006, 97, 13 235502. DOI: http://dx.doi.org/10.1103/PhysRevLett.97.235502

[38] Shvyd'ko Y, Stoupin S, Shu D, Collins SP, Mundboth K, Sutter J, Tolkiehn M. High-contrast sub-millivolt inelastic x-ray scattering for nano- and mesoscale science. Nature Commun. 2014, 5:4219. DOI: 10.1038/ncomms5219

[39] Cai YQ, Coburn DS, Cunsolo A, Keister JW, Honnicke MG, Huang XR, Kodituwakku CN, Stetsko Y, Suvorov A, Hiraoka N, Tsuei KD. The ultrahigh resolution ixs beamline of NSLS-II: Recent advances and scientific opportunities. In: Journal of Physics: Conference Series 2013 (Vol. 425, No. 20, p. 202001). IOP Publishing. DOI: http://dx.doi.org/10.1088/1742-6596/425/20/202001

[40] Suvorov A, Cai YQ, Sutter JP, Chubar O. Partially coherent wavefront propagation simulations for inelastic x-ray scattering beamline including crystal optics. InSPIE Optical Engineering+ Applications 2014 Sep 5 (pp. 92090H-92090H). International Society for Optics and Photonics. DOI: 10.1117/12.2061987

[41] Bermejo FJ, Alvarez M, Bennington SM, Vallauri R. Absence of anomalous-dispersion features in the inelastic neutron-scattering spectra of water at both sides of the melting transition. Phys. Rev. E 1995, 51:2250-2262. DOI: http://dx.doi.org/10.1103/PhysRevE.51.2250

[42] Ruocco G, Sette F. The history of the"fast sound"in liquid water. Condens. Matter Phys. 2008, 11:29-46.

[43] Cunsolo A. The Thz spectrum of density fluctuations of water: The viscoelastic regime. Adv. Cond. Matt. Phys. 2015, 2015:137435. DOI: http://dx.doi.org/10.1155/2015/137435

[44] Ricci MA, Rocca D, Ruocco G, Vallauri R. Collective dynamical properties of liquid water. Phys. Rev. Lett. 1988, 61:1958-1961. DOI: http://dx.doi.org/10.1103/PhysRevLett.61.1958

[45] Pontecorvo E, Krisch M, Cunsolo A, Monaco G, Mermet A, Verbeni R, Sette F, Ruocco, G. High-frequency longitudinal and transverse dynamics in water. Phys. Rev. E 2005, 71:011501. DOI: http://dx.doi.org/10.1103/PhysRevE.71.011501

[46] Petrillo C, Sacchetti F, Dorner B, Suck, JB. High-resolution neutron scattering measurement of the dynamic structure factor of heavy water. Phys. Rev. E 2000, 62:3611-3618. DOI: http://dx.doi.org/10.1103/PhysRevE.62.3611

[47] Sacchetti F, Suck, JB, Petrillo C, Dorner B. Brillouin neutron scattering in heavy water: Evidence for two-mode collective dynamics. Phys. Rev. E 2004, 69:061203. DOI: http://dx.doi.org/10.1103/PhysRevE.69.061203

[48] Cunsolo A, Suvorov A, Cai YQ. The onset of shear modes in the high frequency spectrum of simple disordered systems: Current knowledge and perspectives. Phil. Mag. 2015, 1-11. DOI: 10.1080/14786435.2015.1096975

[49] Sette F, Ruocco G, Krisch M, Masciovecchio C, Verbeni R, Bergmann U. Transition from normal to fast sound in liquid water. Phys. Rev. Lett. 1996, 77:83-86. DOI: http://dx.doi.org/10.1103/PhysRevLett.77.83

[50] Cunsolo A, Kodituwakku CN, Bencivenga F, Frontzek M, Leu BM, Said AH. Transverse dynamics of water across the melting point: A parallel neutron and x-ray inelastic scattering study. Phys. Rev. B 2012, 85:174305. DOI: http://dx.doi.org/10.1103/PhysRevB.85.174305

[51] Cunsolo A, Kodituwakku CN, Bencivenga F, Said AH. Shear propagation in the terahertz dynamics of water-glycerol mixtures. J. Chem. Phys. 2013, 139:184507. DOI: http://dx.doi.org/10.1063/1.4827108

[52] Bove LE, Fabiani E, Fontana A, Paoletti F, Petrillo C, Pilla O, Bento ICV. Brillouin neutron scattering of v-GeO2. Europhys. Lett. 2005, 71:563-569. DOI: http://dx.doi.org/10.1209/epl/i2005-10125-0

[53] Orsingher L, Baldi G, Fontana A, Bove LE, Unruh T, Orecchini A, Petrillo C, Violini N, Sacchetti F. High-frequency dynamics of vitreous GeSe2. Phys. Rev. B 2010, 82:115201. DOI: http://dx.doi.org/10.1103/PhysRevB.82.115201

[54] Scopigno T, Pontecorvo E, Di Leonardo R, Krisch M, Monaco G, Ruocco G, Ruzicka B, Sette, F. High-frequency transverse dynamics in glasses. J. Phys. Condens. Matter 2003, 15:S1269-S1278. DOI: http://dx.doi.org/10.1088/0953-8984/15/11/345

[55] Hosokawa S, Inui M, Kajihara Y, Matsuda K, Ichitsubo T, Pilgrim WC, Sinn H, Gonzalez LE, Gonzalez DJ, Tsutsui S, Baron AQR. Transverse acoustic excitations in liquid Ga. Phys. Rev. Lett. 2009, 102:105502. DOI: http://dx.doi.org/10.1103/PhysRevLett.102.105502

[56] Hosokawa S, Inui M, Kajihara Y, Matsuda K, Ichitsubo T, Pilgrim WC, Sinn H, Gonzalez LE, Gonzalez D.J, Tsutsui S, Baron, AQR. Transverse excitations in liquid Ga. Eur. Phys. J. 2011, 196:85-93. DOI: 10.1140/epjst/e2011-01420-5

[57] Hosokawa S, Munejiri S, Inui M, Kajihara Y, Pilgrim WC, Ohmasa Y, Tsutsui S, Baron AQ, Shimojo F, Hoshino K. Transverse excitations in liquid Sn. J. Phys. Condens. Matt. 2013, 25:112101. DOI: http://dx.doi.org/10.1088/0953-8984/25/11/112101

[58] Hosokawa S, Pilgrim WC, Sinn H, Alp EE. The possibility of transverse excitation modes in liquid Ga. J. Phys. Condens. Matt. 2008, 20:114107. DOI: http://dx.doi.org/10.1088/0953-8984/20/11/114107

[59] Giordano VM, Monaco G. Inelastic x-ray scattering study of liquid ga: Implications for the short-range order. Phys. Rev. B 2011, 84:052201. DOI: http://dx.doi.org/10.1103/PhysRevB.84.052201

[60] Paciaroni A, Orecchini A, Haertlein M, Moulin M, Conti Nibali V, De Francesco A, Petrillo C, Sacchetti F. Vibrational collective dynamics of dry proteins in the terahertz region. J. Phys. Chem. B 2012, 116:3861-3865. DOI: 10.1021/jp211190q

[61] Violini N, Orecchini A, Paciaroni A, Petrillo C, Sacchetti F. Neutron scattering investigation of high-frequency dynamics in glassy glucose. Phys. Rev. B 2012, 85: 134204. DOI: http://dx.doi.org/10.1103/PhysRevB.85.134204

[62] Li MD, Chu XQ, Fratini E, Baglioni P, Alatas A, Alp EE, Chen SH. Phonon-like excitation in secondary and tertiary structure of hydrated protein powders. Soft Matter 2011, 7:9848-9853. DOI: 10.1039/C1SM05954H

[63] Ruocco G, Sette F, Bergmann U, Krisch M, Masciovecchio C, Mazzacurati V, Signorelli G, Verbeni R. Equivalence of the sound velocity in water and ice at mesoscopic wavelengths. Nature 1996, 379:521-523. DOI: 10.1038/379521a0

[64] Renker B. Phonon dispersion in D2O-ice. Phys. Lett. A 1969, 30:493-494. DOI:

[65] Monaco G, Cunsolo A, Ruocco G, Sette F. Viscoelastic behavior of water in the terahertz-frequency range: An inelastic x-ray scattering study. Phys. Rev. E 1999, 60:5505-5521. DOI: http://dx.doi.org/10.1103/PhysRevE.60.5505

[66] Bafile U, Guarini E, Barocchi F. Collective acoustic modes as renormalized damped oscillators: Unified description of neutron and x-ray scattering data from classical fluids. Phys. Rev. E 2006, 73:061203. DOI: http://dx.doi.org/10.1103/PhysRevE.73.061203

[67] Mountain RD. Spectral Distribution of Scattered Light in a Simple Fluid. Rev. Mod. Phys. 1966, 38:205-214. DOI: http://dx.doi.org/10.1103/RevModPhys.38.205